Article

Local Microstructure and Texture Development during Friction Stir Spot of 5182 Aluminum Alloy

Thierry Baudin [1], Sandrine Bozzi [2], François Brisset [1] and Hiba Azzeddine [3,*]

[1] CNRS, Institut de Chimie Moléculaire et des Matériaux d'Orsay, Université Paris-Saclay, 91405 Orsay, France; thierry.baudin@universite-paris-saclay.fr (T.B.)
[2] Aubert & Duval, Rue du Villa, 63770 Les Ancizes, France; sandrine.bozzi@eramet.com
[3] Laboratory of Materials and Renewable Energy, Faculty of Sciences, Mohamed Boudiaf University, M'sila 28000, Algeria
[*] Correspondence: hiba.azzeddine@univ-msila.dz

Abstract: The local microstructure, texture gradient and mechanical properties through the shoulder dimension (10 mm) of upper and lower AA5182 aluminum sheets were investigated using electron backscatter diffraction (EBSD) and Vickers microhardness after friction stir spot welding (FSSW). Based on the microstructural features (mean grain size, grain boundary type and dynamic recrystallization (DRX)), the upper sheet was found to be mainly composed of the stir zone (SZ) and thermomechanically affected zone (TMAZ) due to the high deformation induced simultaneously by the tool rotation and the shoulder download force, while the SZ, TMAZ, heat-affected zone (HAZ) and base metal (BM) were detected in the lower sheet due to the limited effect of the shoulder on the lower sheet. The texture changes, due to the nature of the deformation, demonstrated a shear-type texture at the SZ to a plane strain compression deformation type texture at the TMAZ and then a recrystallization texture at the HAZ and BM. The microhardness gradually decreased with the increasing distance from the keyhole along the SZ, TMAZ and HAZ regions. Eventually, the microstructure and microhardness evolutions were correlated based on the Hall–Petch relationship.

Keywords: aluminum; EBSD; friction stir spot welding; microstructure; texture

1. Introduction

Aluminum (Al)-based alloys are widely used in transportation industries owing to their attractive properties such as high strength-to-weight ratio, high electrical and thermal conductivities and good corrosion resistance [1–3]. Today, friction stir welding (FSW) and friction stir spot welding (FSSW) techniques are frequently used in automotive and aerospace structural applications, especially in materials with poor weldability by conventional fusion welding such as aluminum or titanium alloys [3–11].

During FSW, a non-consumable tool formed of a shoulder and a pin is rotated and plunged into two sheets and then translated in one direction. The combination of plastic deformation and frictional heat induced by the rotating tool guarantees the bonding between the two sheets by the formation of a solid-state weld [4,5,12]. The processing of FSSW is similar to FSW but without the tool turning [13]. Therefore, FSSW involves three steps: plunging, bonding and drawing out, which result in the formation of a keyhole in the middle of the joint [14]. Consequently, FSW and FSSW produce a complex microstructure in the welded material that can be divided into four distinct regions: (1) the base metal (BM), (2) the heat-affected zone (HAZ), (3) the thermomechanically affected zone (TMAZ) and (4) the stir zone (SZ) [10,15,16]. The material in the SZ undergoes both severe plastic deformation and high temperature after the friction stir, which results in excellent grain refinement due to the occurrence of dynamic recrystallization (DRX). In the TMAZ, the material suffers from plastic deformation and heating but it is insufficient for DRX; hence, this zone is usually characterized by a highly deformed microstructure. In the HAZ,

the material is only affected by heat generated during welding and the microstructure, especially the grain size, is similar to that of the BM. Finally, the BM is far away from the weld and it is not affected by deformation or heating [10,16,17]. The crystallographic texture can change through the weld joint, depending on the nature of the deformation processing. Numerous papers can be found focusing only on the characterization of the texture in the SZ that developed a shear texture type [18–23]. However, reports on the characterization of the texture in the TMAZ and HAZ are very limited [9,21,24]. It is expected that the HAZ has a similar texture to the BM and the texture of the TMAZ is more complicated due to the heterogeneous plastic flow [9,21,24].

The heterogeneity of the microstructure and grain orientation (crystallographic texture) along these zones directly affects the mechanical properties of the welded material and therefore its performance [23]. Moreover, the final material will strongly depend on the initial state in terms of grain size, grain morphology, the distribution and fraction of the second phases [25–27]. Hence, in recent decades, various research and experimentation has been conducted to elucidate the mechanisms responsible for the microstructural and textural evolution [18–23,28–33], fractures [13,15,34] and material flow [14,21,35] during processing and much of it has focused on the optimization of FSW parameters such as tool rotation speed, downward force and tool geometry to improve the mechanical properties and decrease the anisotropy in the welded materials [12,13,17,36–44].

For example, it was observed that the shear strength of the FSSW Al 5182 alloy is significantly improved by increasing the rotational speed up to 1300 rpm [13]. In this case, the high heat generated from the rotational speed causes the enlargement of the SZ and assures good bonding [13]. Despite the various investigations, much work is still needed for a full understanding of the microstructural and especially textural evolution of FSSW and its associated mechanisms, notably in the TMAZ and HAZ.

Hence, the aim of the present study is the evaluation of the local textural and microstructural evolution of the SZ, TMAZ, HAZ and BM through the shoulder dimension of the upper and lower Al5182 sheets after FSSW. In addition, the mechanical properties obtained through the distribution of Vickers microhardness along the distance from the keyhole center of the upper and lower sheets were correlated to these metallurgical evolutions. Finally, the contribution of grain size strengthening to the local mechanical properties was estimated by the Hall–Petch relationship [45,46]. It is believed that the present results can promote microstructure and texture control during the FSSW of non-treatable Al-based alloys.

2. Materials and Methods

The chemical composition of the AA5182-O alloy is summarized in Table 1.

Table 1. Chemical composition in weight percentage of AA5182-O alloy.

Mg	Fe	Mn	Zn	Si	Cu	Cr	Ti	Al
4.5	0.35	0.35	0.25	0.2	0.15	0.1	0.1	balance

The FSSW was conducted using an AA5182 upper sheet 1.2 mm thick and an AA 5182 lower sheet 2 mm thick. Note that the sheet reference frame is defined as rolling direction (RD), transverse direction (TD) and normal direction (ND). A cylindrical threaded pin (3.5 mm diameter and 1.8 mm height) and flat shoulder (diameter 10 mm) fabricated of steel Z38CDV5 treated at 50HRC was used for the welding.

The welding was realized with clamping force of 6 kN, rotation speed of 1300 rpm and plunge time of 2.5 s. These parameters were selected based on a previous study in which the AA5182 joint weld exhibited good mechanical properties [13].

The local microstructure and texture analysis through the FSSW joints were carried out by EBSD measurements on the longitudinal cross-section (RD-ND plane), which is normal to the welding direction (WD), i.e., the vertical axis in Figure 1. Figure 1 shows the scanning

electron microscope (SEM) micrograph of the longitudinal cross-section of AA 5182 after FSSW and the EBSD scanning positions at the upper (y = 1 mm) and lower (y = 0 mm) sheet, respectively. As indicated in the Figure 2, the measurements were performed at the right (x = 2, 2.5, 3, 3.5, 4 and 5 mm) and left (x = −2, −2.5, −3, −3.5, −4 and −5 mm) sides on both sheets from the keyhole centre (x = 0 mm), respectively. The scale value was positive on the right side and negative on the left side.
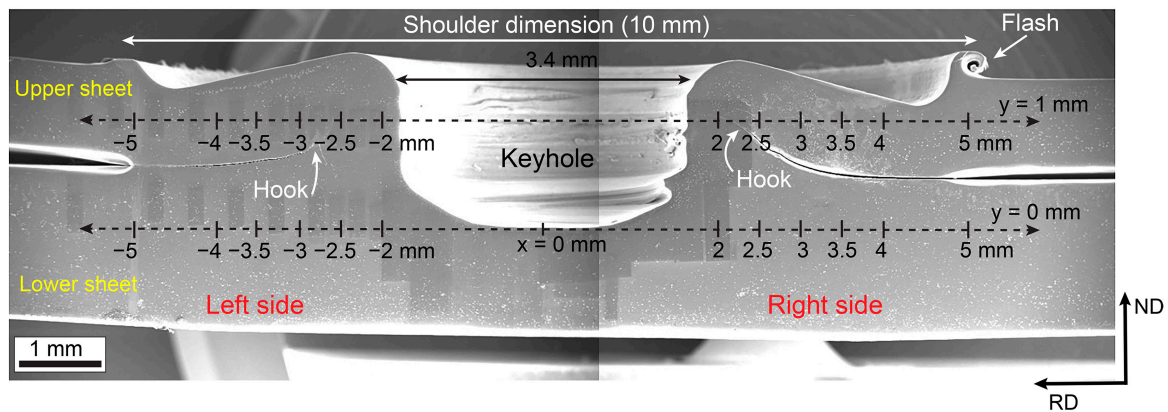

Figure 1. The SEM micrograph of the longitudinal cross-section of Al 5182 alloy after FSSW and the EBSD scanning positions.

After the FSSW, a keyhole is formed at the centre of the FSSW joint due to the pin morphology. In addition, an amount of flash can be seen at the upper sheet (see arrow) resulting from the penetration of the shoulder, which is expected during the FSSW [41]. The SEM micrograph also shows the formation of a hook (see Figure 2), which is the interface between the upper and lower sheets near the SZ and is bent upwards towards the upper sheet owing to the combination of plunging and stirring effects during welding [44]. The bonding at the interfaces of the upper and lower sheets seems better on the left side.

The EBSD sample preparation consists of mechanical polishing followed by electrolytical polishing at 20 °C with a Struers A2 solution adapted to Al-based alloys with a voltage of 45 V over 12 s. The EBSD measurements were performed using a TSL-EDAX-Hikari system mounted on a scanning electron microscope FEG-SEM ZEISS Supra 55 VP operating at 20 kV. The acquisition and analysis of the scan areas of about $200 \times 200 \ \mu m^2$ with a step size of 0.5 and/or 0.6 μm were processed by Orientation Imaging Microscopy, OIM^{TM} software.

The grain size data were obtained using a grain tolerance angle of 5° and a minimum grain size of 5 pixels. All datum points with a confidence index (CI) lower than 0.05 were excluded from the quantitative analyses, where CI quantifies the reliability of the indexed pattern [47]. The mean grain size was measured using the equivalent diameter approach. Grain boundaries with misorientation angles $\theta < 2°$ were excluded from EBSD maps to avoid spurious boundaries caused by orientation noise [48]. Based on that, the grain boundary types were divided into sub-grain boundaries or very low angle grain boundaries (VLAGBs) with misorientation $2° < \theta < 5°$, low angle grain boundaries (LAGBs) with $5° < \theta < 15°$ and high angle grain boundaries (HAGBs) with $\theta > 15°$, respectively.

The grain orientation spread (GOS) and the kernel average misorientation (KAM) approaches implemented in OIM™ software were used to estimate the distribution of plastic deformation of a grain by measuring its local misorientation. Grain orientation spread is defined as the average deviation between the orientation of each point in the grain and the average orientation of the grain, where grains with GOS lower than 1° are considered strain-free grains (undeformed or fully recrystallized grains) [49]. Grain orientation spread value increases due to the development of misorientation within the grain resulting from the accumulation of dislocations. In the present case, the grains were separated into three groups: (1) undeformed or recrystallized grains having GOS value

in the range of 0–1°, (2) partially deformed or recovered grains having GOS value in the range of 1–2° and (3) deformed grains having GOS > 2°.

Kernel average misorientation is known as the average misorientation angle of a given point with all its neighbors belonging to the same grain [50]. Here, the θ_{KAM} value was calculated from the mean misorientation angle between a given point and its 3th neighbors excluding misorientations greater than 5°. Hence, the dislocation density can be obtained following the equation [50]:

$$\rho = \frac{\alpha \theta_{KAM}}{ndb} \tag{1}$$

where $\alpha = 3$ for mixture of tilt and twist boundary types, $b = 0.28$ nm is the Burgers vector, $n = 3$ for the third neighbor and d is the scan step size.

MTEX software was used to analyze the evolution of texture in the different locations by calculating the orientation distribution function (ODF) using the harmonic method (L = 22) and a gaussian function with a half-width of 5° to model each orientation [51].
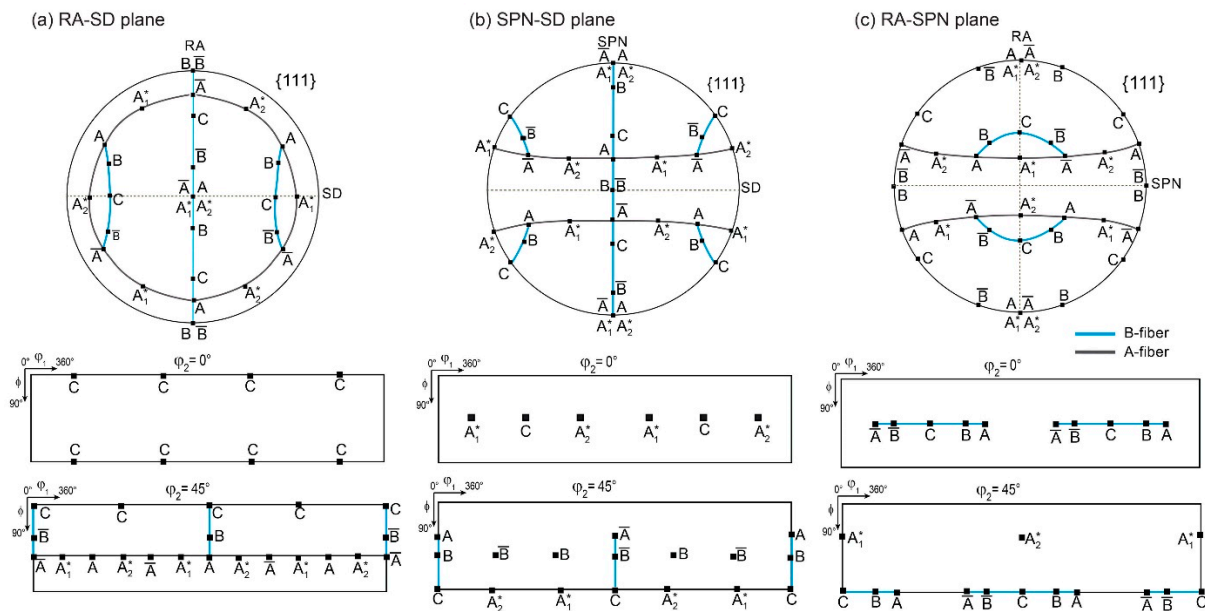

Figure 2. {111} pole figures and ODF sections at $\varphi_2 = 0$ and 45° displaying the positions of the ideal shear texture components on: (**a**) RA-SD, (**b**) SPN-SD and (**c**) RA-SPN planes for materials with FCC structure [52].

The measured texture in the TMAZ, HAZ and BM regions is presented in the observed RD-ND plane. For the SZ, it is well documented that the shear texture reference frame is not constant and changes with the rotation of the tool [9,11,19]. Accordingly, in the transverse cross-section of the weld material (TD-ND plane), the shear direction (SD) is tangential to the tool surface, the shear plane normal (SPN) is perpendicular to the tool surface and rotation direction axis (RA) is aligned with the inclined vertical surface of the tool [9,11,19]. Usually, rotations are performed around the reference directions (RD, TD, or ND) of the EBSD measurement to match the shear texture developed in the SZ with the ideal reference frame SPN-SD plane.

In the present case, the textures of the SZ regions are presented in RD-ND plane and the identification of the different shear texture components of the obtained {111} pole figure and ODF is simply performed by a direct comparison with the ideal shear component positions in the different RA-SD, SPN-SD and RA-SPN planes [52] as shown in Figure 2. The positions of ideal shear texture components for face-centered cubic (FCC) materials projected in RA-SD, SPN-SD and RA-SPN planes are summarized in Table 2 [52]. The shear texture in FCC materials is formed typically from A-fiber ({111}//SP) composed

of A, $\bar{A}$, A_1^* and A_2^* components and *B*-fiber (<110>//SD) comprised of A, $\bar{A}$, B, $\bar{B}$ and C components [52]. It is believed that the presentation of the SZ texture in the RD-ND plane (EBSD measurement plane) can be used to track the material flow within the weld.

Table 2. Position of ideal shear texture components for FCC materials projected in RA-SD, SPN-SD and RA-SPN planes [52].

Notation	RA-SD Plane		SPN-SD Plane		RA-SPN Plane	
	Miller index {hkl}<uvw>	Euler angles (°) (φ_1, Φ, φ_2)	Miller index {hkl}<uvw>	Euler angles (°) (φ_1, Φ, φ_2)	Miller index {hkl}<uvw>	Euler angles (°) (φ_1, Φ, φ_2)
A	{$\bar{1}11$}<110>	(60, 54.7, 45)	{112}<$\bar{1}10$>	(0, 35.2, 45)	{110}<$\bar{1}\bar{1}2$>	(54.7, 90, 45)
$\bar{A}$	{$1\bar{1}\bar{1}$}<$\bar{1}10$>	(120, 54.7, 45)	{211}<$0\bar{1}1$>	(50.7, 65.9, 63.4)	{101}<$\bar{1}\bar{2}1$>	(35.26, 45, 90)
A_1^*	{$1\bar{1}1$}<112>	(90, 54.7, 45)	{101}<$\bar{1}\bar{2}1$>	(35.26, 45, 90)	{121}<$\bar{1}0\bar{1}$>	(129.23, 65.9, 26.5)
A_2^*	{$11\bar{1}$}<$\bar{2}\bar{1}1$>	(30, 54.7, 45)	{011}<$\bar{2}\bar{1}1$>	(144.7, 45, 0)	{211}<$0\bar{1}1$>	(50.7, 65.9, 63.4)
B	{$1\bar{1}2$}<110>	(50.7, 65.9, 63.4)	{111}<$\bar{1}10$>	(0, 54.7, 45)	{110}<$\bar{1}\bar{1}1$>	(35.26, 90, 45)
$\bar{B}$	{$\bar{1}\bar{1}2$}<$\bar{1}\bar{1}0$>	(0, 35.26, 45)	{111}<$0\bar{1}1$>	(60, 54.7, 45)	{101}<$\bar{1}\bar{1}1$>	(54.7, 45, 90)
C	{001}<110>	(45, 0, 0)	{110}<$\bar{1}\bar{1}0$>	(0, 90, 45)	{011}<$0\bar{1}1$>	(90, 45, 0)

The microhardness distributions on the longitudinal cross-section of each sheet were obtained using a Vickers microhardness tester (LECO M400H) with a 50 g load for 20 s and a spacing of 0.5 mm along the y = 0 (lower sheet) and 1 mm (upper sheet) lines (Figure 1), respectively.

3. Results

3.1. Microstructure and Texture of BM

Figure 3 presents the orientation imaging micrography (OIM) in inverse pole figure (TD-IPF) and GOS maps of the BM of the upper and lower sheets, respectively. The HAGBs are indicated by black lines. The mean grain size and fraction of recrystallized grains are shown in the upper part of the TD-IPF and GOS maps. Both sheets exhibit a typical static recrystallization microstructure formed of equiaxed and recrystallized grains (about 91 and 96%) with mean grain size of 19.5 μm in the upper sheet and 16.6 μm in the lower sheet. These differences are obviously due to the thermomechanical forming processes. The initial textures of both sheets are presented in Figure 3 via {111} pole figure and ODF sections at φ_2 = 0 and 45°, respectively. The ideal deformation and recrystallization textures of the rolled FCC alloys are also shown in Figure 3 and their descriptions in the RD-ND plane are given in Table 3. The texture of the upper sheet is dominated by the Cube component while the texture of the lower sheet exhibits the presence of static recrystallization components (Cube, Goss (G_1) and rotated Goss (G_2)) and the retained deformation Brass (Bs) component. The presence of retained deformation texture components such as Brass or Copper is often reported in hot-rolled Al-based alloys [53–56].
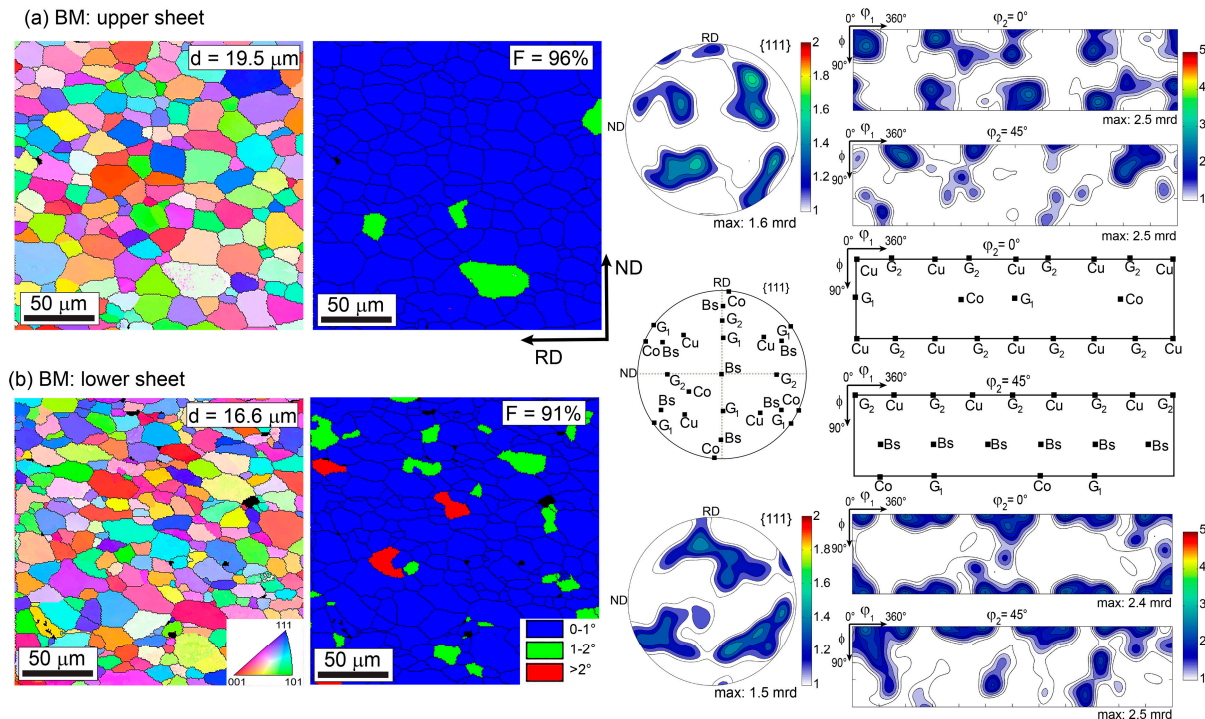
Figure 3. The TD-IPF, GOS maps, {111} pole figure and ODF sections at $\varphi_2 = 0$ and $45°$ of BM: (**a**) upper sheet and (**b**) lower sheet. Ideal texture component positions are shown for comparison.

Table 3. Position of ideal deformation and recrystallization texture components for rolled FCC materials projected in RD-ND plane.

Notation	RD-ND Plane	
Rolling component	Miller index {hkl}<uvw> *	Euler angles (°) (φ_1, Φ, φ_2)
Brass (Bs)	$\{111\}<\bar{1}\bar{1}2>/\{111\}<11\bar{2}>$	(90, 55, 45)/(270, 55, 45)
Copper (Co)	$\{110\}<1\bar{1}1>$	(30, 90, 45)
Goss 1 (G_1)	$\{011\}<100>$	(0, 45, 0)
Goss 2 (G_2)	$\{001\}<110>$	(45, 0, 0)
Cube (Cu)	$\{001\}<0\bar{1}0>$	(90, 0, 0)

* {hkl}//(RD, ND) plane and <uvw>//RD.

3.2. Microstructure and Texture Evolution after FSSW

3.2.1. Microstructure Evolution after FSSW

Figures 4 and 5 present the evolution of the microstructure via TD-IPF and GOS maps of the upper and lower sheets as a function of distance from the keyhole center of the welded Al 5182 alloy. In both sheets and both sides, the TD-IPF maps show that the microstructure is significantly heterogeneous along the shoulder diameter. Basically, the microstructure is formed from fine grains near the keyhole corresponding to the SZ and the grain size increases with increasing distance from the keyhole center. A significant texture gradient along the distance from the keyhole center is also noticed. The evolution of texture is presented in the next section. The GOS maps indicate that the fine grains are mostly fully recrystallized (having GOS 0–1°) and deformed grains (having GOS > 2°) appear with increasing distance typically belonging to the TMAZ, followed by large grains mostly recovered (green grains, having GOS 1–2°) belonging to the HAZ, and finally the microstructure in some places, such as at x = −5 mm (left side) and x = 5 mm (right side) of the lower sheet, is fully recrystallized, which corresponds to the BM. It is interesting

to note that the BM is not reached in the upper sheet through the entire distance (up to x = −5 and 5 mm).
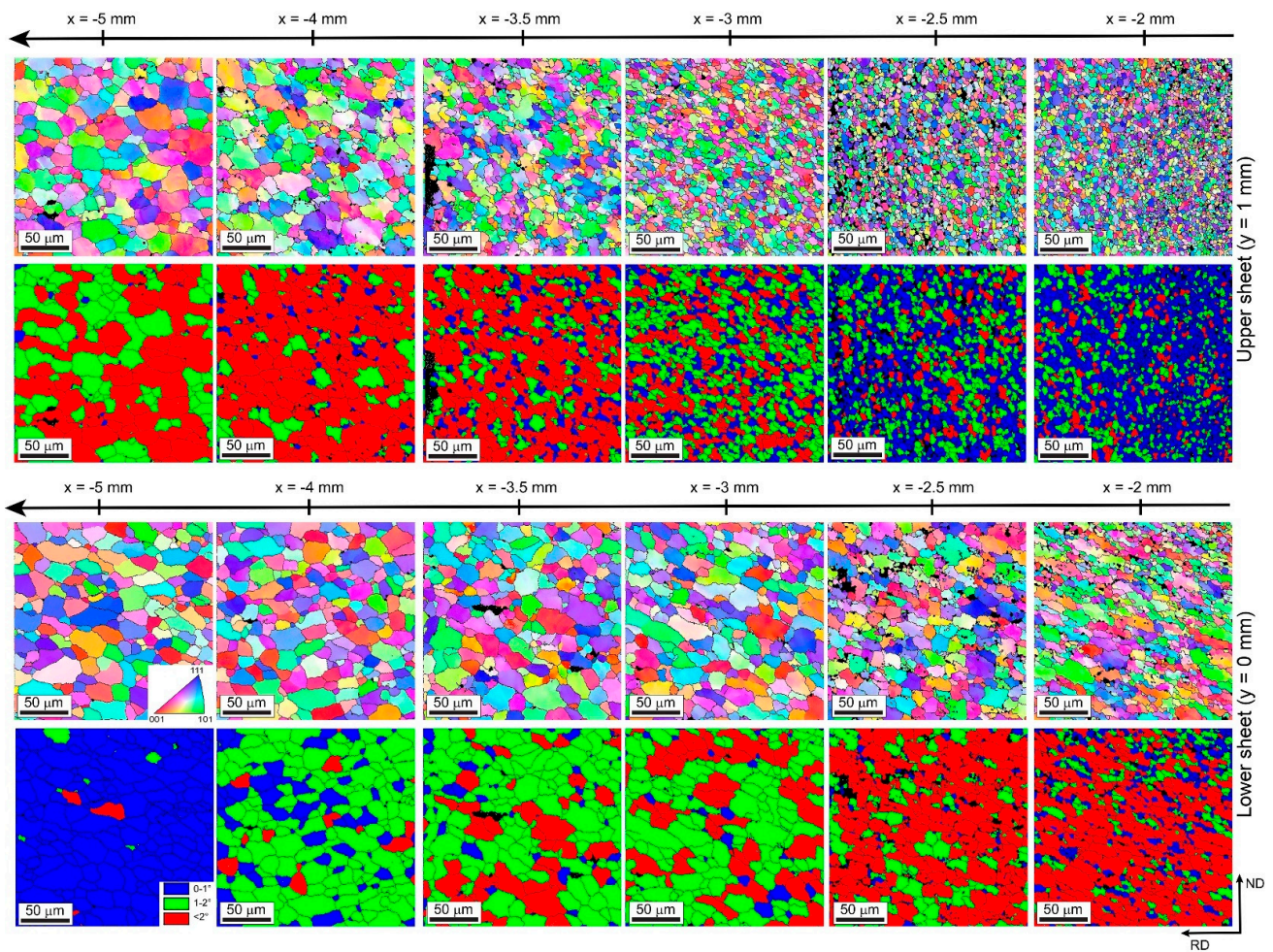

Figure 4. The TD-IPF and GOS maps showing the evolution of the microstructure as a function of distance from the center of the keyhole (left side) at upper sheet (y = 1 mm) and lower sheet (y = 0 mm), respectively.

For more details, the evolution of mean grain size, DRX (GOS 0–1°), recovered or partially deformed (GOS 1–2°) and deformed (GOS > 2°) grain fractions, VLAGBs, LAGBs and HAGBs at different locations are shown in Figure 6. Based on the microstructural variations, the different joint zones in the upper and lower sheets are identified and highlighted in the plots shown in Figure 6.

Globally, the upper sheet along the shoulder diameter is formed of 50% SZ, 41.6% TMAZ and 8.4% HAZ, while the lower sheet is composed of 16.7% SZ, 25% TMAZ, 41.6% HAZ and 16.7% BM. Two main differences can be noticed in the weld joints. First, the deformation is more pronounced in the upper sheet than in the lower sheet and second the microstructure evolution is not symmetrical at the right and left sides of the weld.
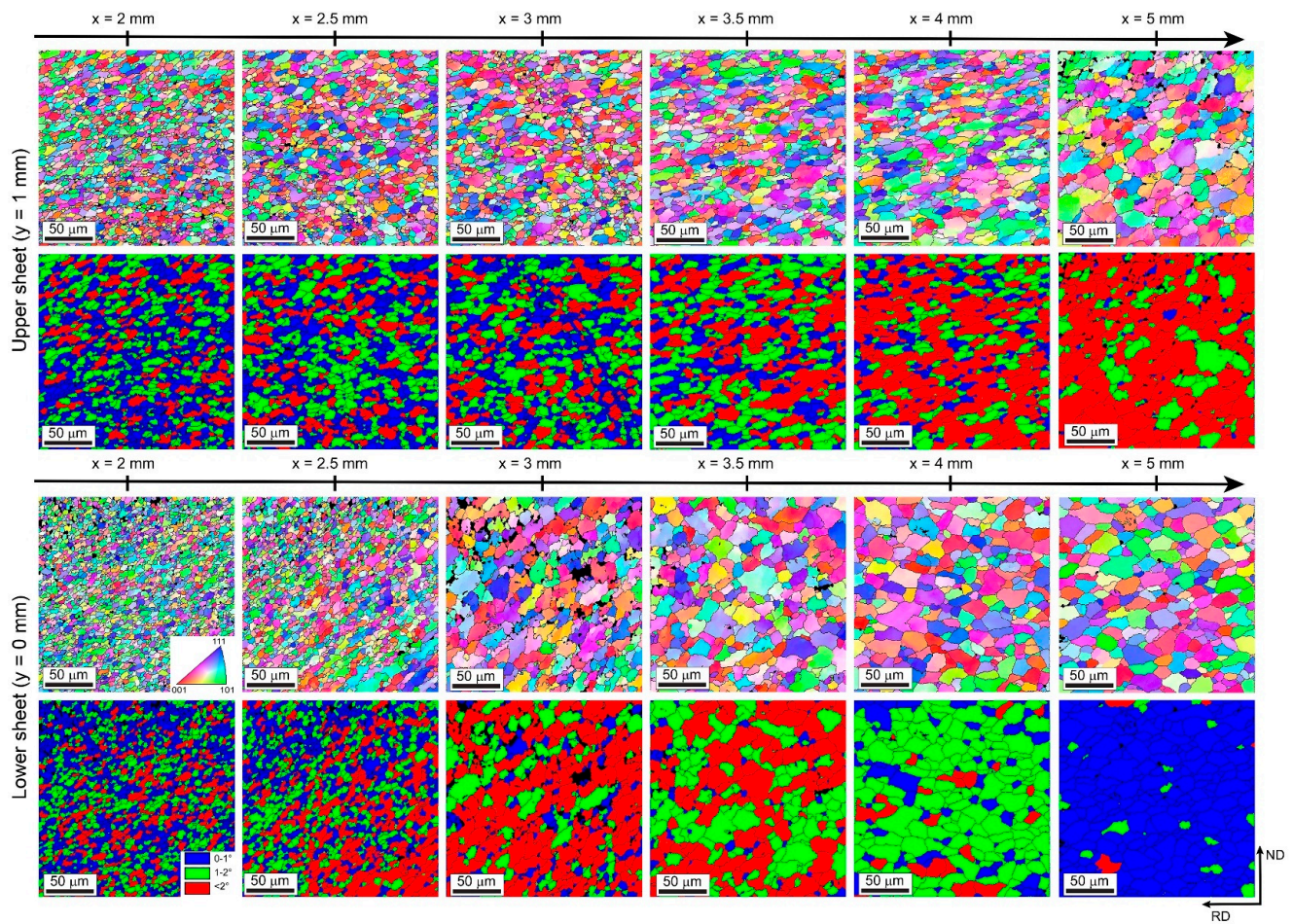
Figure 5. The TD-IPF and GOS maps showing the evolution of the microstructure as a function of distance from the center of the keyhole (right side) at upper sheet (y = 1 mm) and lower sheet (y = 0 mm), respectively.

The first difference can be evidenced by the evolution of microstructural parameters shown in Figure 6. Indeed, the right side of the lower sheet contains the four typical joint zones: SZ, TMAZ, HAZ and BM. In this area, the mean grain size increases with increasing distance from the keyhole (SZ and TMAZ) and then saturates when it reaches the HAZ and BM. The fraction of DRX (GOS 0–1°) decreases with increasing distance from the keyhole between the SZ and TMAZ and then increases in the HAZ region to reach a high fraction of about 94% at the BM. It is interesting to note that the HAZ region is characterized by a high fraction of partially deformed grains (green grains, GOS 1–2°). The HAGB fraction decreases with increasing distance and then rapidly increases when it reaches the HAZ and continues to increase at the BM. Consequently, the fractions of VLAGBs and LAGBs increase between the SZ and TMAZ due to the generation of dislocations and their rearrangement and then decrease when reaching the HAZ and BM.

Meanwhile, the evolution of the microstructural features at the right side of the upper sheet, such as the continuous decrease in DRX and HAGB fractions up x = 5 mm, indicates the presence of only the SZ and TMAZ regions. It seems that the SZ and TMAZ width is larger in the upper sheet due to the extra severe plastic deformation induced by the download force of the shoulder (compression deformation).
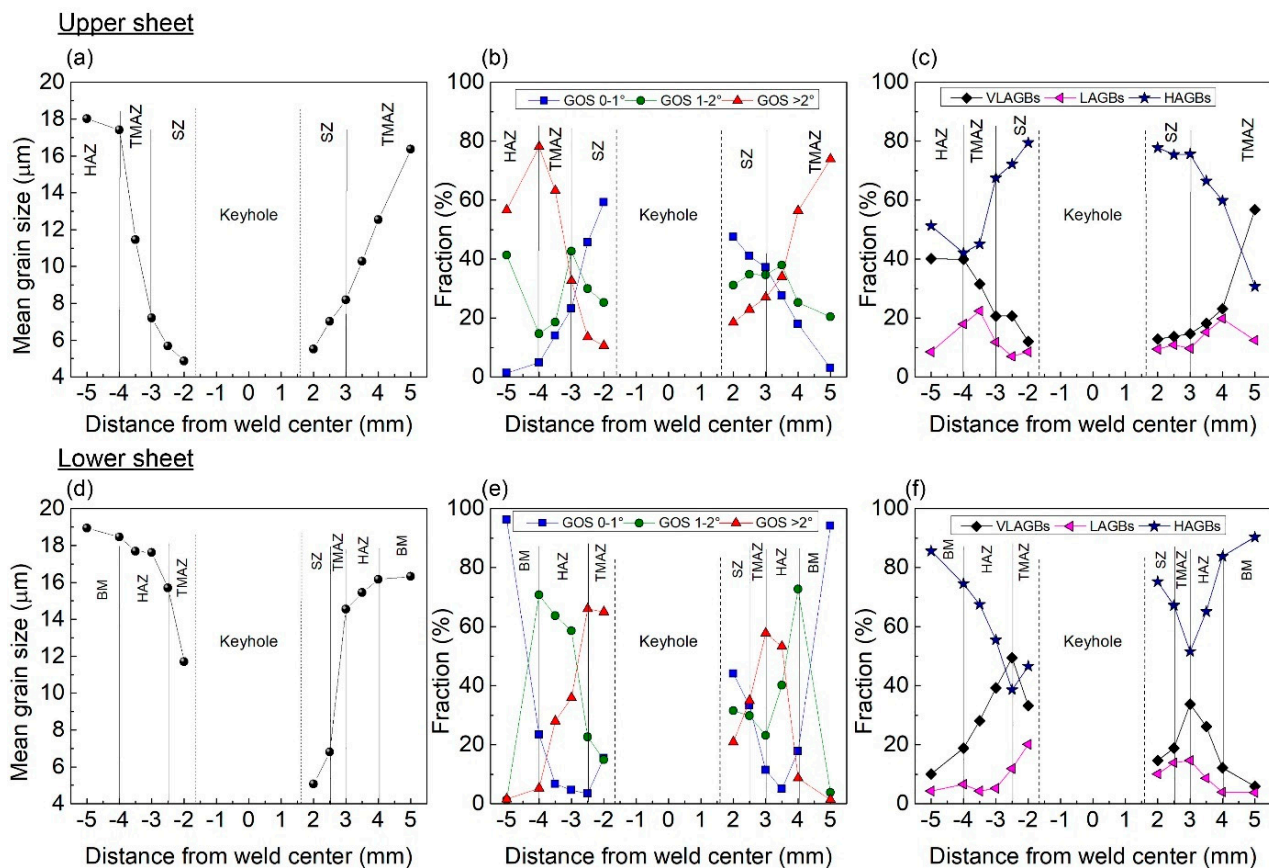
Figure 6. Evolution of (**a**,**d**) mean grain size, (**b**,**e**) DRX (GOS 0–1°), partially deformed (GOS 1–2°) and deformed (GOS > 2°) grain fractions and (**c**,**f**) grain boundary types (VLAGBs, LAGBs and HAGBs) as a function of distance from the keyhole center at the upper and lower sheet, respectively.

Concerning the second noted difference, for example, the SZ is not detected at x = −2 mm of the lower sheet (Figure 4) since the large mean grain size (*d* = 11.7 μm) and the low fraction of DRX (15.4%) recorded in this position indicate that this area belongs to the TMAZ rather than the SZ. Moreover, on the left side of the upper sheet, the width of the TMAZ (1 mm) is smaller than for the right side (about 2 mm). The change of the joint weld on both sides may indicate that the right side undergoes more deformation than the left side. Such differences could be created due to the nature of the stirring process and the tool movement on both sides. This is similar to the heterogeneity observed between the advancing and retreating sides in the conventional FSW technique [57].

3.2.2. Texture Evolution after FSSW

Figures 7 and 8 present the texture evolution via {111} the pole figure and ODF sections at $\varphi_2 = 0$ and 45° as a function of distance from the center of the keyhole at the upper sheet (y = 1 mm) and lower sheet (y = 0 mm), respectively. The positions of ideal shear and rolling texture components in {111} the pole figure and ODF sections at $\varphi_2 = 0$ and 45° of FCC materials are shown in Figures 2 and 3 and their descriptions are given in Tables 2 and 3, respectively.
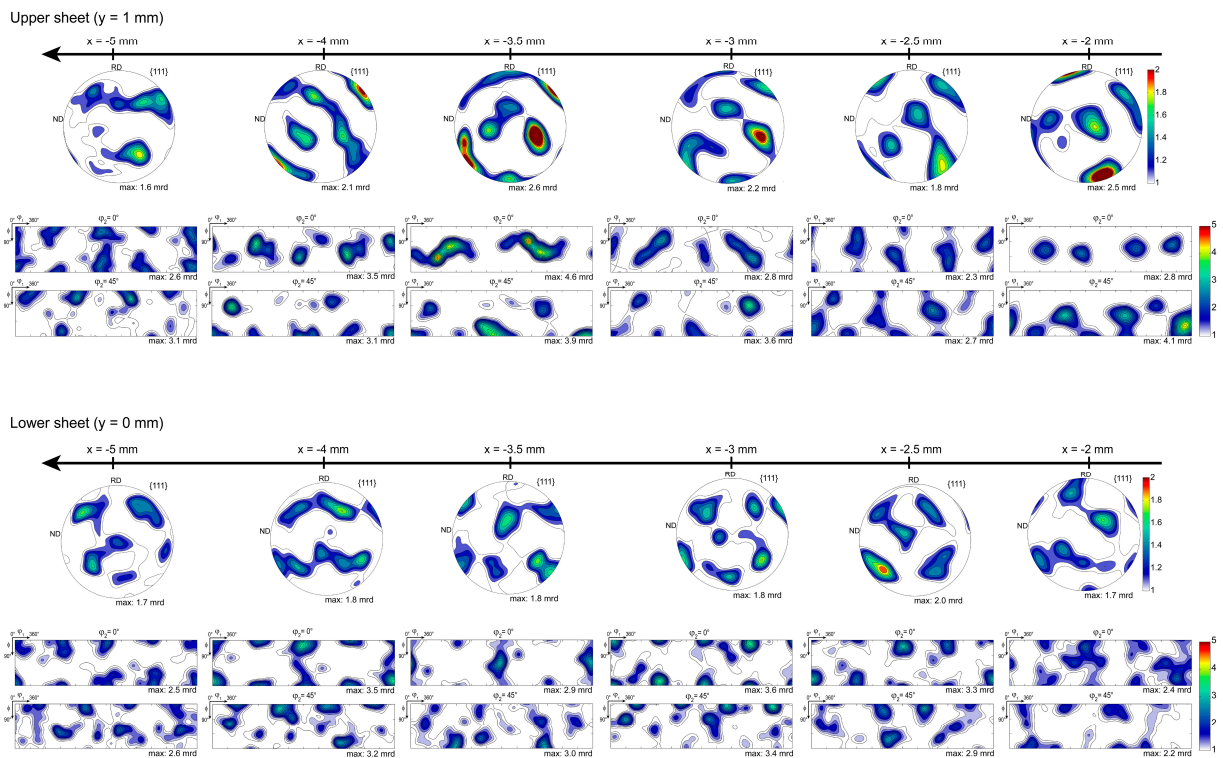
Figure 7. {111} pole figure and ODF sections at $\varphi_2 = 0$ and $45°$ showing the texture evolution as a function of distance from the center of the keyhole (left side) at upper sheet (y = 1 mm) and lower sheet (y = 0 mm), respectively.

Figure 8. {111} pole figure and ODF sections at $\varphi_2 = 0$ and $45°$ showing the texture evolution as a function of distance from the center of the keyhole (right side) at upper sheet (y = 1 mm) and lower sheet (y = 0 mm), respectively.
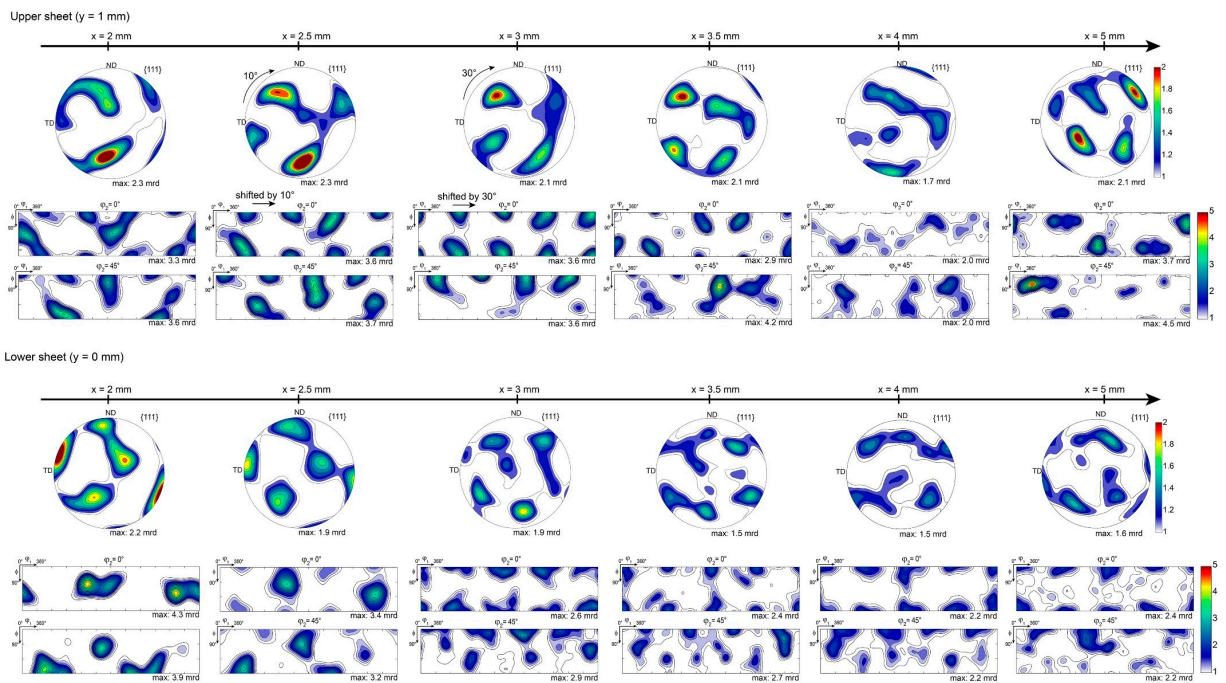
There is the obvious development of a pronounced texture gradient in the upper and lower sheets through the distance from the keyhole center. It is clear from Figures 7 and 8 that the textural characteristics near the keyhole (SZ) are typical of simple shear deformation. Then, the texture gradually transforms from shear texture to typical plane strain compression texture with increasing distance from the keyhole center (TMAZ, HAZ and BM).

Based on Figure 2, the positions of the shear texture components of the SZ for the left side (at x = −2 and −2.5 mm) of the upper sheet show that the RD-ND plane is parallel to the SPN-SD plane, while their positions at the right side (at x = 2, 2.5 and 3 mm) change to the RA-SD plane (RD-ND//RA-SD). For the lower sheet, the shear texture is located only at the right side (at x = 2 and 2.5 mm) and their positions indicate that the RD-ND plane is aligned with the RA-SPN plane. The identification of different texture components through the joints and the positions is complicated; hence, Table 4 summarizes the major texture components developed in the SZ, TMAZ, HAZ and BM.

Table 4. The main texture components developed in different areas of the welded Al 5182 alloy.

	SZ	TMAZ	HAZ	BM
Upper sheet				
Left side	C, B, A, A_2^*, Cu and G_1 (at 2–3 mm)	Co and G_1 (at 3.5–4 mm)	Cu and G_1 (at 5 mm)	—
Right side	C, B, A and G_1 (at 2–3 mm)	Cu, G_1 and Bs (at 3.5–5 mm)	—	—
Lower sheet				
Left side	—	Cu, Co and G_1 (at 2 mm)	Cu, G_1 and Bs (at 2.5–4 mm)	Cu and Bs (at 5 mm)
Right side	A, B, A_2^* and G_1 (at 2–2.5 mm)	Cu and Bs (at 3 mm)	Cu, G_1 and Bs (at 3.5–4 mm)	Cu (at 5 mm)

The texture of the SZ at the upper sheet exhibits the presence of C, A, B, A_2^*, shear components and recrystallization texture components such as Cube and Goss components. The SZ of the lower sheet seems to show similar texture evolution except for the absence of C and Cube components. Local texture inhomogeneity is detected in the SZ. For example, the texture is gradually rotated about the TD at x = 2 mm (about 10°) and at x = 3 mm (about 30°) from the keyhole center as shown on the right side of the upper sheet (see Figure 8). The instability of the shear texture of the SZ through the distance is widely reported in various welded materials and it is explained by the complexity of deformation and strain heterogeneity induced by the tool geometry [9,18,20–23,32,33,43].

The typical shear texture disappears at the TMAZ regions and is replaced by a typical texture for plane strain compression with the development of Copper and Brass components. It is interesting to note that the recrystallization texture components (Cube and Goss) are still present in the TMAZ regions. The texture of the HAZ regions is characterized by the presence of Cube, Goss and Brass (only in the lower sheet) components that are very similar to the texture of both BMs (Figure 3). The texture differences between the upper and lower sheets can also be related to the initial texture of both BM sheets (Figure 3).

3.3. Microhardness Evolution

Figure 9 displays the evolution of microhardness as a function of distance from the keyhole center for the upper and lower sheets, respectively. The SZ, TMAZ, HAZ and BM regions are highlighted in the microhardness plots. The microhardness of the BM is about 80 HV.
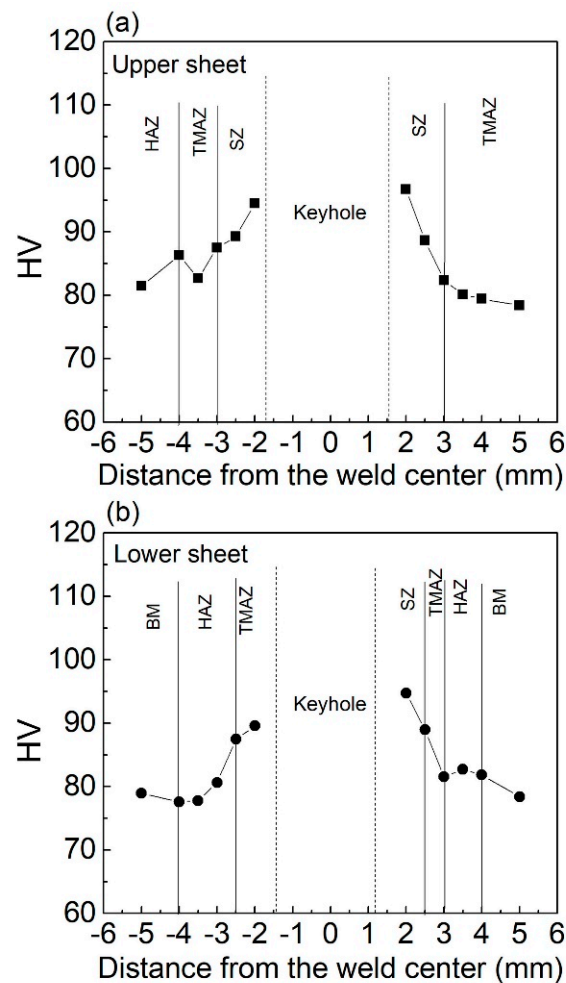
Figure 9. Microhardness evolution as a function of distance from the keyhole center for: (**a**) upper and (**b**) lower sheet.

The highest value of microhardness of about 95 HV is detected in the SZ (at x = 2 mm from the keyhole center) of both sheets due to the development of grain refinement. Then, the microhardness gradually decreases with increasing distance from the keyhole along the TMAZ and HAZ regions. The high values of the TMAZ in comparison with those for the HAZ regions can be explained by the increase in dislocation density due to the plastic deformation during the FSSW. The microhardness of the HAZ is similar to the BM in the lower sheet, reaching a value of 80 HV. The range of microhardness variation of several Al-based alloys is found around 67–110 HV through the SZ, TMAZ, HAZ and BM regions [58–61].

4. Discussion

The evolution of the microstructure and texture along the shoulder dimension of the upper and lower sheets of the welded Al 5182 alloy was found to be very heterogeneous due to the development of different zones (SZ, TMAZ, HAZ and MB). Below, each joint zone of the weld alloy is discussed separately.

4.1. Microstructure and Texture Evolution in Different Joint Zones
4.1.1. The SZ Region

The width of the SZ in the upper sheet coincides with the region where the upper and lower sheets are bonded (as can be seen in Figure 1). The grain refinement is very rapid due to the severe plastic deformation and heating, which makes the identification of DRX

mechanisms impossible. However, many investigations demonstrated that, for materials with high stacking fault energy such as Al, the continuous DRX (CDRX) mechanism is responsible for grain refinement [30]. The grain size recorded in the SZ of the upper sheet (4.8 μm at x = −2 mm and 5.5 μm at x = 2 mm from the keyhole center) was similar to that for the SZ in the lower sheet (5.0 μm at x = 2 mm), which may indicate that the shoulder contact on the upper sheet does not affect the grain structure of the SZ.

The microstructure of the SZ in the upper sheet is characterized by an onion ring structure resulting from the periodical deposition of material layers. The presence of an onion ring structure in the SZ is the most characteristic feature of friction stir welds. In general, the formation of such a specific structure is caused by the rotation of the tool and the forward movement extrudes the metal around to the retreating side of the tool [40,62–66]. It was proposed in the case of the FSW technique that the onion ring structure starts on the retreating side of the weld and competes with tunnel defects originating at the advancing side of the weld [63]. Consequently, the formation of a noticeable onion ring structure indicates fewer tunnel defects [63]. Some investigations showed that the onion ring structure is more noticeable on the advancing side than on the retreating side of the weld [63,65]. Principally, the rotation and translation of the tool have the same direction in the advancing side, which causes an increase in strain and heat, while the rotation and translation directions are the opposite on the retreating side, which leads to a lower strain [57]. However, other investigations observed that the onion ring structure was more located on the retreating side of the weld [40]. The definition of advancing and retreating sides cannot be used in FSSW since the translation movement is absent. However, it is obvious that in the present case the onion ring structure is more pronounced on the right side than on the left side of the upper sheet. The location of the onion ring seems to depend on the tool geometry and its interaction with the material [40,63].

Figure 10 shows more detailed microstructural and textural examinations of the onion ring structure formed in the SZ region of the upper sheet located at x = 2 mm (right side) from the keyhole center. Figure 10 shows the onion ring structure in which the two materials of the upper and lower sheets are well mixed. However, there is the obvious formation of large and small bands with a thickness approximately equal to 12.1 and 4.5 μm, respectively. In addition, the small bands contain fine grains with a mean grain size lower than 4.5 μm, while the mean grain size of the large bands is higher than 4.5 μm.

The GOS map of the zoomed area shown by the black frame displays that the grains of the small bands are fully recrystallized, while the majority of the grains belonging to the large bands are partially or completely deformed. The texture evolution shown by the ODF sections at $\varphi_2 = 0$ and 45° in both bands is slightly different. Moreover, with the domination of *C* and Goss components in both bands, grains in the small bands develop a rotated Cube component (R-Cube {110}<1–10>, (0°, 90°, 45°)). The rotated Cube component is known as a typical recrystallization texture component often developed in FCC materials, while the SZ of the lower sheet shows no evidence of an onion ring structure. In addition, the SZ on the left side of the lower sheet is not detected at 2 mm from the keyhole center, indicating that the material in this region was not reached by the rotation of the tool.
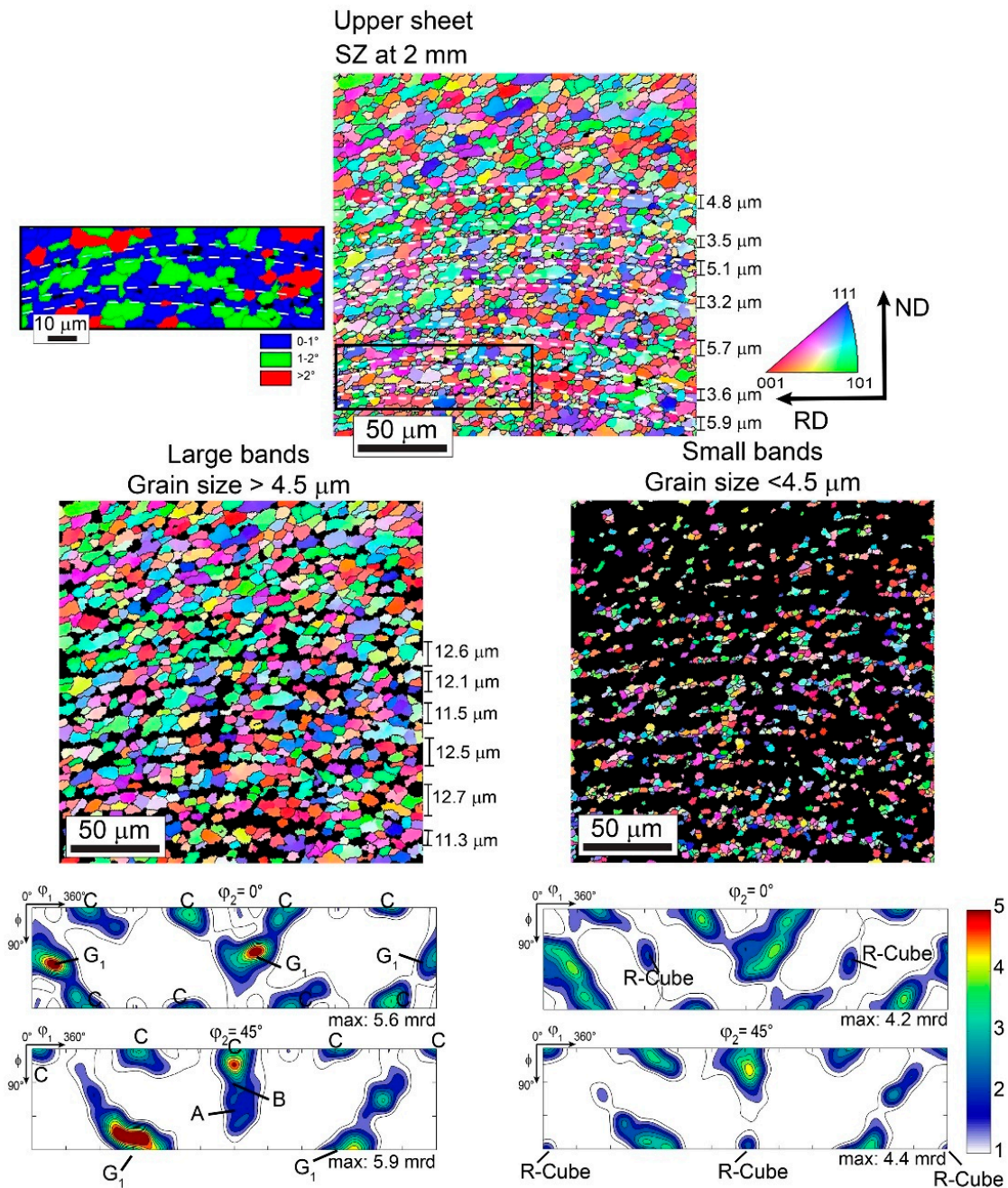
Figure 10. The TD-IPF maps, GOS map of the zoomed area and ODF sections at φ₂ = 0 and 45°
showing the microstructure and texture of large and small bands belonging to the onion ring structure
of SZ region at 2 mm from the center of the keyhole (right side) of the upper sheet, respectively.

The SZ of the upper sheet is characterized by the development of *C*, *B* and *A* components. In addition, the left side shows the presence of the A_2^* component. Concerning the lower sheet, the shear-type texture, formed of *A*, *B* and A_2^* components, is located only on the right side, which is in good agreement with the evolution of microstructural parameters (Figures 5 and 6). In addition, the *C* component seems absent in the SZ of the lower sheet compared with the upper sheet. This difference could be related to the local shear strain. For example, it was reported that the *B* component transformed into the *C* component under shoulder rotation [22]. This is seemingly in accordance with the present results, since the shoulder is not in direct contact with the lower sheet. The presence of the *C* and A_1^*/A_2^* components may indicate that the material has undergone a small amount of

shear strain, while the development of the $B/\bar{B}$ components means that the material has experienced a high magnitude of shear strain [18,21]. Accordingly, the AA 5182 present has been subjected to medium shear strain in the SZ.

It is noteworthy that the Goss component is also present in all of the SZ. The Cube component is also detected in the SZ left side of the upper sheet. In addition, the R-Cube is detected in the small bands (Figure 10). The presence of these texture components in the SZ has rarely been reported in FSW Al-based alloys [28]. It is well known that the development of these texture components is characteristic of the occurrence of static recrystallization. It seems that the heat generated from tool rotation is high enough to cause static recrystallization. The temperature cycle during the FSSW of AA 5182 recorded at the periphery of the tool (keyhole border) is shown in Figure 11. As can be seen, the temperature increases rapidly up to 320 °C then slowly increases to reach a maximum value of 418 °C. The peak temperature reached is in the range of the recrystallization temperature of the AA 5xxx series [67–69]. Hence, it is expected that static recrystallization will occur during the FSSW in which typical recrystallization texture components such as Cube, R-Cube, Goss and R-Goss can be generated.
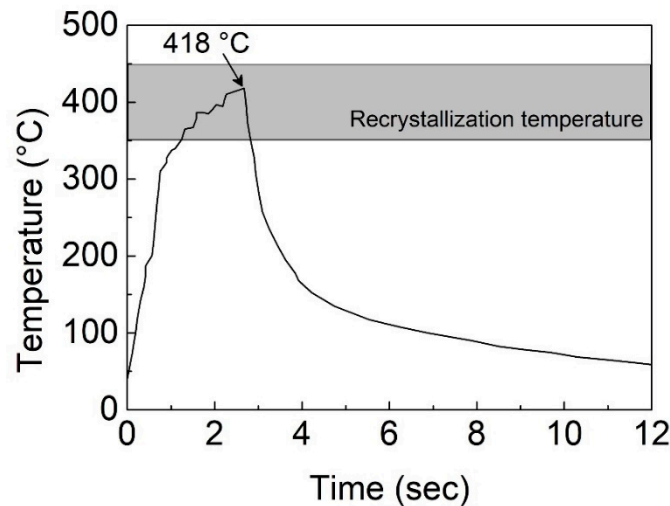

Figure 11. Temperature cycle during the FSSW of AA 5182 recorded at the periphery of the tool (keyhole border) [38].

4.1.2. The TMAZ Region

The width of the TMAZ was not the same in the upper and lower sheets or on the left and right sides. The larger width of 1.5 mm (from 3.5 to 5 mm) was located on the right side of the upper sheet, while the thin widths of 0.5 mm and 1 mm were located on the right side (from 2.5 to 3 mm) and left side (from 1.5 to 2.5 mm) of the lower sheet, respectively. This could be attributed to the download force imposed mainly on the upper sheet by the shoulder. The fractions of VLAGBs and HAGBs are higher in this region in comparison with the SZ and HAZ (Figure 6). The microstructure of the TMAZ near the SZ is mainly characterized by elongated deformed grains (having GOS > 2°) and some small, recrystallized grains (having GOS 0–1°) located at the grain boundaries. This is characteristic of discontinuous DRX (DDRX) [70]. Examples are shown in the zoomed area of regions at −3.5 mm in the upper sheet and −2.0 mm in the lower sheet as indicated in Figure 12. Most of the grain boundaries (GBs) are serrated due to the difference in dislocation density between the two sides of the grain boundaries. The misorientation between the serrated GB and deformed grains increases, leading to the development of sub-grain boundaries (VLAGBs) that transform into LAGBs and then into small grains with HAGBs as indicated by the white arrows in Figure 12. The corresponding {111} pole figures of deformed and DRX grains shown in Figure 12 indicate that DRX grains globally develop a similar texture to the deformed grains.
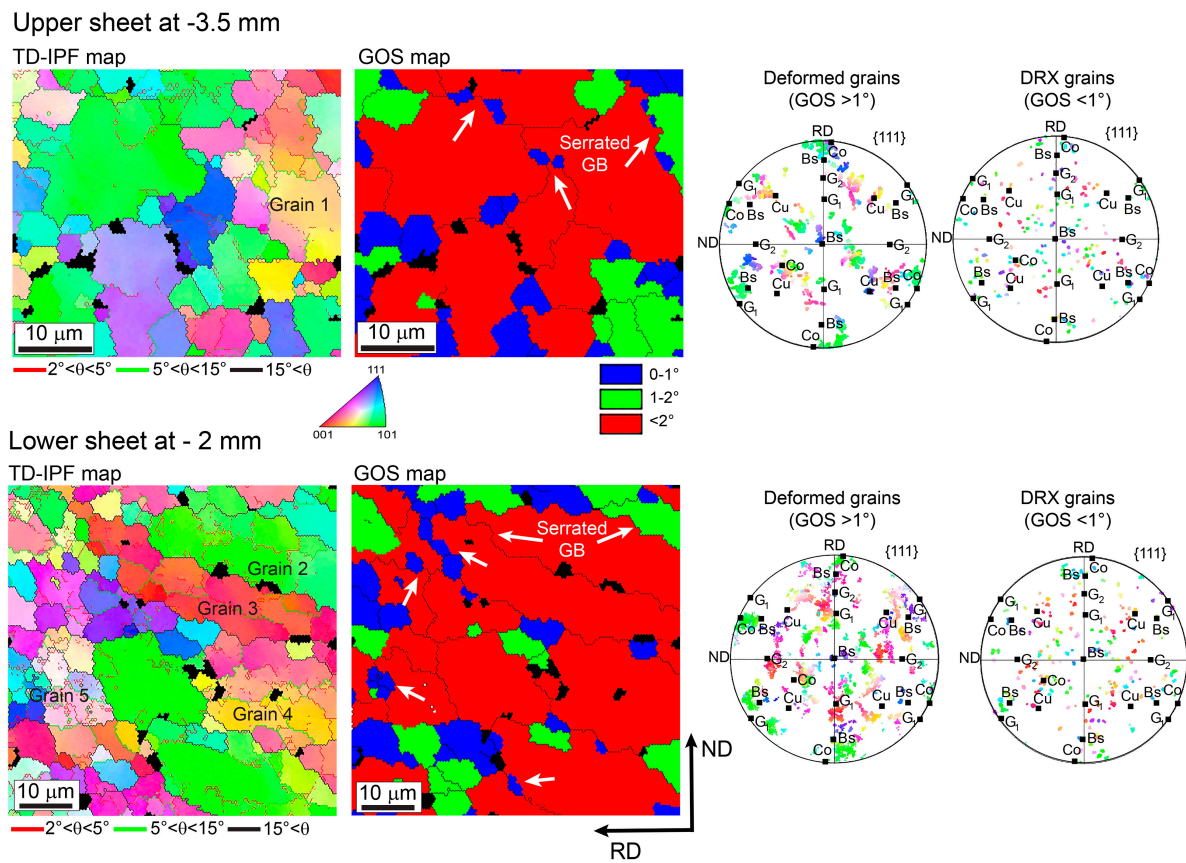
Figure 12. The TD-IPF, GOS maps and the corresponding {111} pole figures of deformed and DRX grains of TMAZ regions at −3.5 mm (left side) of the upper sheet and at −2 mm (left side) of the lower sheet, respectively.

The DRX is very weak in these regions and the deformed grain fraction (GOS > 2°) in the TMAZ (Figure 6) increases with increasing distance from the keyhole center, demonstrating that the effect of the heat generated from the tool rotation decreases with increasing distance and hence prevents the occurrence of DRX. The elongated deformed grains are mostly fragmented and contain a relatively high fraction of VLAGBs and LAGBs inside them (see grains 1–5 in Figure 12). This is a characteristic of CDRX through the sub-grain development (SGD) mechanism [70]. It is evident that the stored energy depends on the grain orientation. For example, the fraction of LAGBs is higher in grains 4 and 5 than in grain 2. Several investigations demonstrated the dependency of stored energy on the crystallographic texture in conventional and severely deformed FCC materials [52,71–74].

It is worth noting that the SGD mechanism can maintain the orientation of the deformed grains (see grains 2 and 3) or can gradually change the orientation of the subsequent segments from the original orientation, as can be noticed in grains 1, 4 and 5 in Figure 12. This explains the persistence of orientations such as Cube and Goss, while the presence of the texture gradient explains the development of complex rolling textures (mostly deviated from their ideal positions) observed in the TMAZ region, especially along the upper sheet (Figure 8).

4.1.3. The HAZ Region

Details characteristic of the evolution of the microstructure and texture in the HAZ are not well documented in the literature. The HAZ is defined as a region from the weld joint in which the microstructure is only affected by the heat generated by the tool; hence, it is expected that the microstructure and the texture will be quite similar to the BM but with a larger grain size due to the grain growth process. This may explain the decrease in dislocation density in the HAZ compared to the BM of naturally aged AA 6063 [32]. Nevertheless, experimental results demonstrated that the grain size of the HAZ was found to be lower than for the BM in welded aluminum_steel joints and this was explained by the use of low welding temperatures [31].

In the present case, the mean grain size of the HAZ was very similar to the BM (Figure 6) but with a significant increase in the GOS value; i.e., the majority of the HAZ grains are partially deformed (green grain, GOS 1–2°), which means the presence of dislocation activity in the HAZ region compared to the BM.

To quantify the amount of strain (dislocation density) in the HAZ region, the KAM maps of regions located at x = −3.5 and x = −4 mm from the keyhole center of the lower sheet (left side) are shown in Figure 13. The KAM map of BM (at x = −5 mm) is also calculated for comparison and shown in Figure 13. It is obvious that the microstructure of the HAZ is more deformed than the BM and the deformation increases with increasing distance from the BM. It seems that the distortion in the HAZ at x = −4 mm started at the triple junction where sub-grain boundaries with misorientation of 2–5° start to accumulate as indicated by arrows in the grain boundary type map of the zoomed area (red box). Then, the number of sub-grain boundaries increases and propagates along the entire grain of the HAZ at x = −3.5 mm as indicated in the zoomed area (yellow box). The dislocation density was calculated based on Equation (1) and the results are shown in Figure 13. The dislocation density of the BM is about 6.7×10^{13} m^{-2} and it increases to 9.3 and 12×10^{13} m^{-2} at x = −4 and −3.5 mm, respectively. Such results demonstrate that the HAZ suffers from some amount of deformation. Further investigations are needed to explore the source of the strain distribution near the HAZ regions.

In contrast, the texture evolution of the HAZ and BM seems very similar and shows principally the presence of the Cube, Goss and Brass components (Table 4). The evolution of the volume fractions of these components is shown in Figure 14. The volume fractions of the texture components were calculated with an orientation tolerance of 15° from their ideal position. The fraction of the Brass component is similar in the three positions. The Cube component first increases at x = −4 mm and then decreases at x = −3.5 mm, while the fraction of the Goss component increases in both HAZ regions.

To identify the orientation of the different grains in both HAZ regions (at x = −3.5 and −4 mm of the lower sheet), their microstructures are partitioned as grains having GOS values of 0–1°, 1–2° and >2° and their corresponding textures are shown in Figure 15. The number of grains with GOS 0–1° (DRX grains) and GOS >2° (deformed grains) were very low in the region at x = −3.5 and −4 mm, respectively; hence, they were not implemented in Figure 15. As can be observed, the grains with GOS = 0–1°, considered fully recrystallized, have Cube and rotated Goss (G_2) orientations. This result explains the decrease in the Cube texture component in the HAZ at x = −3.5 mm since the DRX is restricted, while the orientations of grains with GOS = 1–2° for both regions change to near Goss and Brass orientations. The Brass and Goss components are still present in grains with higher deformation (GOS > 2°). In addition, grains with a new orientation located near the Copper one, as indicated by its ideal position in the ODF sections, are developed by crystal lattice rotation induced by slip processing [75]. The Copper orientation is known as a deformation texture component in FCC materials. In addition, the Copper texture component was observed in the TMAZ region.
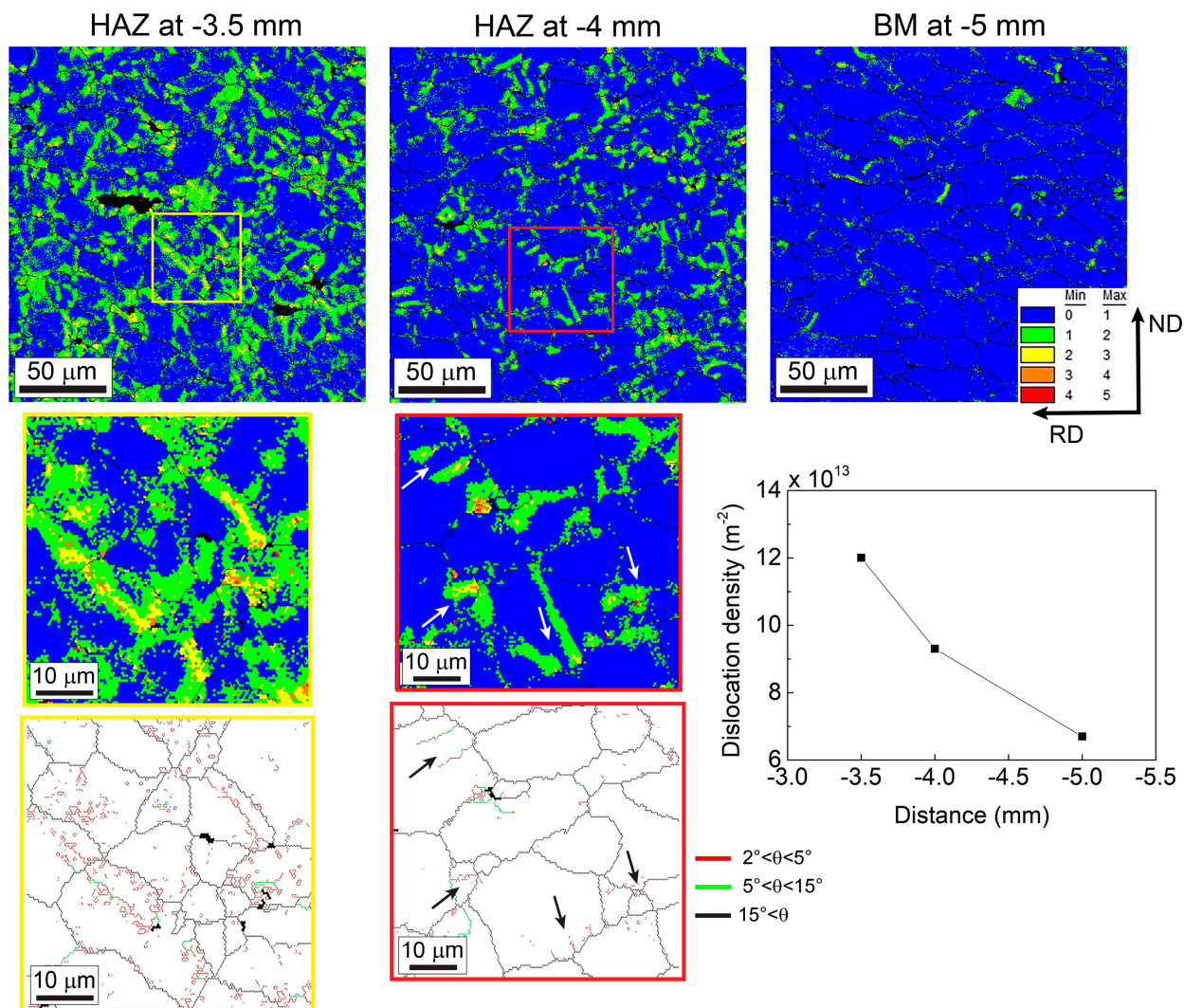
Figure 13. The KAM maps of HAZ regions at −3.5 and −4 mm and BM (at −5 mm) of the lower sheet (left side) and the evolution of dislocation density in these regions.
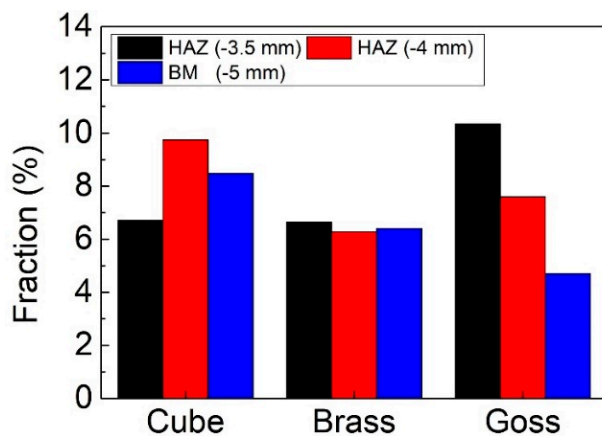

Figure 14. Evolution of volume fraction of Cube, Brass and Goss components in HAZ at x = −3.5 and −4 mm and BM at −5 mm from the keyhole center of the lower sheet (left side).
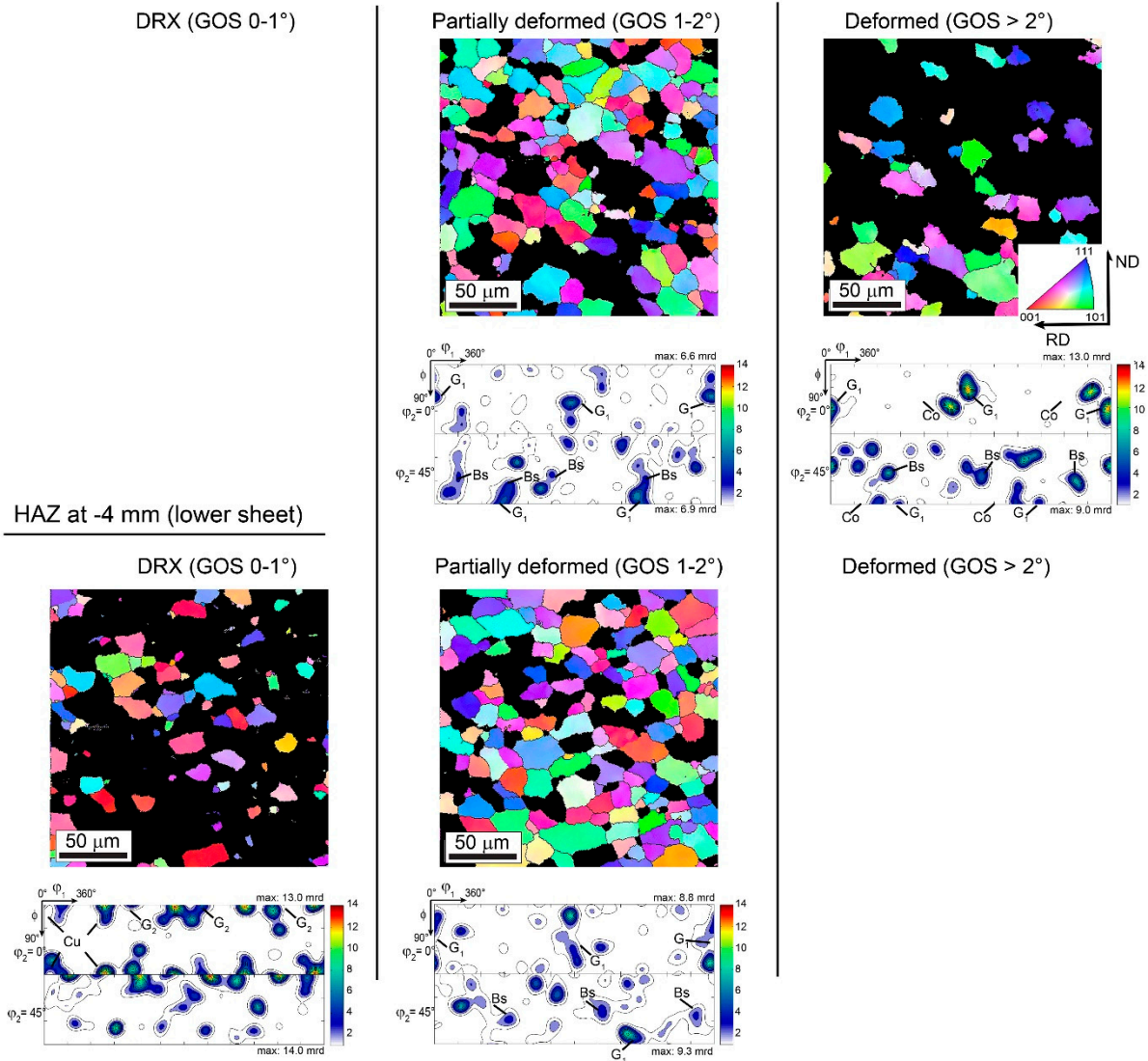
Figure 15. The TD-IPF maps and ODF sections at $\varphi_2 = 0$ and $45°$ showing the microstructure and texture of DRX (GOS 0–1°), partially deformed (GOS −1–2°) and deformed grains (GOS > 2°) of HAZ regions at x = −3.5 and −4 mm from the center of the keyhole (left side) of the lower sheet, respectively.

It is worth noting that the HAZ width of the lower sheet is quite similar on the left (from x = −2.5 to −4 mm) and right sides (from x = 3 to 4 mm) and the microstructural and textural characteristics are very similar, which indicates a homogeneous heat coupled with the same amount of deformation input during the welding. Meanwhile, the HAZ in the upper sheet is located only at x = −5 mm from the keyhole center (left side). The microstructure and texture of this zone are slightly different from those of the lower sheet. For example, the Brass component is absent in comparison with the HAZ of the lower sheet. This is expected, since the microstructures of the BM of the upper and lower sheets are slightly different, as already shown in Figure 3.

4.1.4. The BM Region

The evolution of the microstructure and texture revealed that the BM was not reached along the shoulder dimension (10 mm) in the upper sheet, while the BM in the lower sheet was detected at x = −5 and 5 mm (the extremity of shoulder dimension) due to the absence

of the download force of the shoulder. To localize the BM in the upper sheet, additional EBSD measurements were performed at x = 5.5 and 6 mm (on the left and right sides) from the keyhole center, and the corresponding microstructures (TD-IPF and GOS maps) and textures (ODF sections at $\varphi_2 = 0$ and $45°$) are shown in Figure 16. As can be seen, the microstructures and textures at x = −5.5 and 5.5 mm still exhibit the characteristics of the HAZ region and then the BM is attained at x = −6 and 6 mm from the keyhole center.

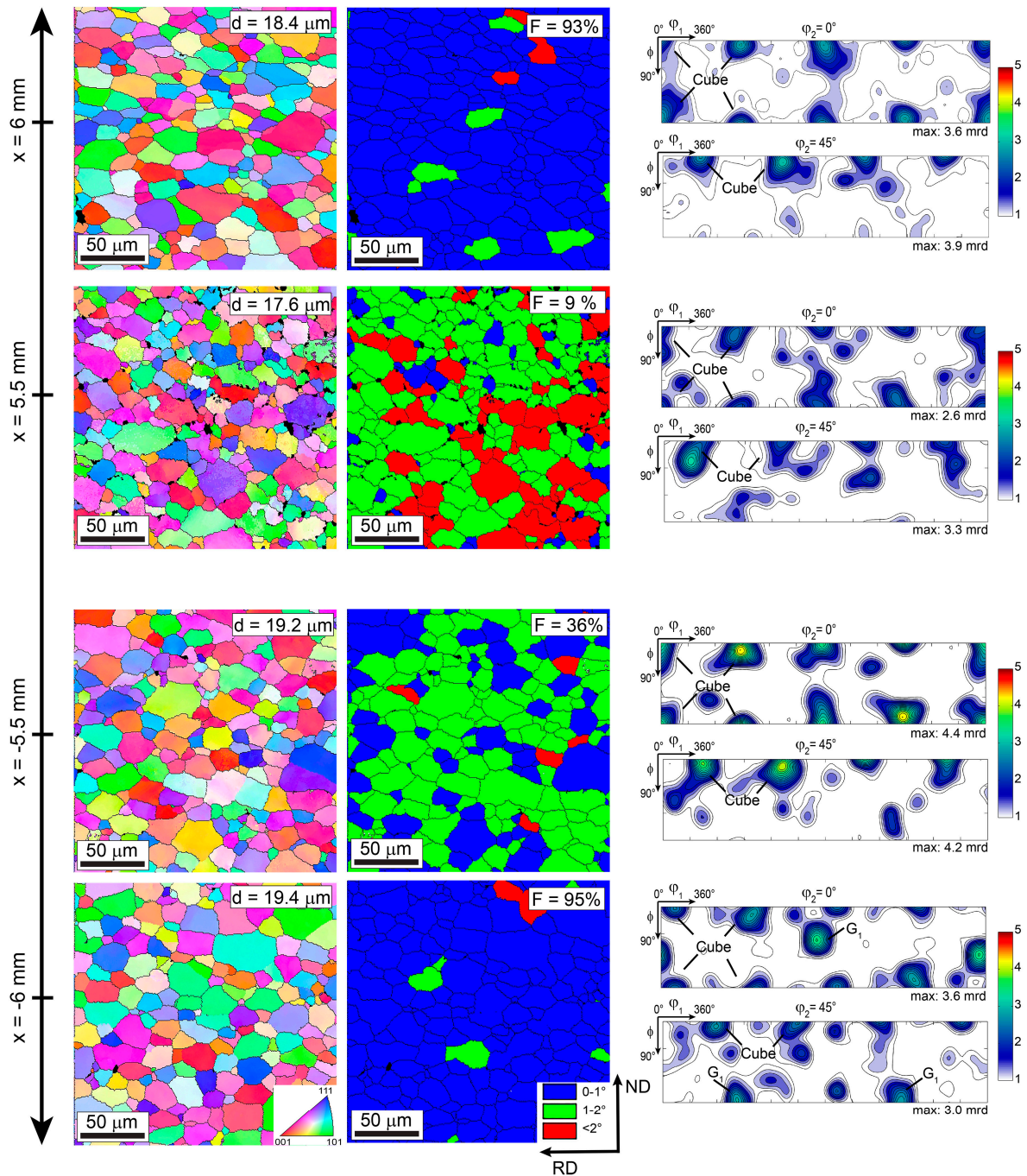**Figure 16.** The TD-IFP, GOS maps and ODF sections at $\varphi_2 = 0$ and $45°$ showing the evolution of microstructure and texture of regions at 5.5 and 6 mm (left and right sides) from the keyhole center of the upper sheet.

4.2. Relationship between Microstructure and Mechanical Properties of the Joint

It is interesting to note that the microhardness difference between the different zones (SZ, TMAZ and HAZ and BM) is not sharp, which may assure good deformation compatibility between the joint and the BM.

The hardening induced by the deformation processing of materials is generally attributed to the concomitant occurrence of dislocation hardening and grain size hardening [76]. Based on the microstructural evolution discussed earlier, it can be concluded that the grain size hardening is more important through the joint (BM, HAZ, TMAZ and SZ) than dislocation hardening.

For further analysis, the microhardness values were plotted as a function of the reciprocal of the square root of the mean grain size for the different (BM, HAZ, TMAZ and SZ) welded zones following the Hall–Petch equation [45,46] and the result is shown in Figure 17:

$$H_v = H_{v0} + \frac{k_H}{\sqrt{d}} \tag{2}$$

where H_{v0} is the friction hardness associated with the resistance of the crystal lattice to the movement of dislocations and k_H is a Hall–Petch constant, which indicates the contribution of the grain boundaries to the hardening.
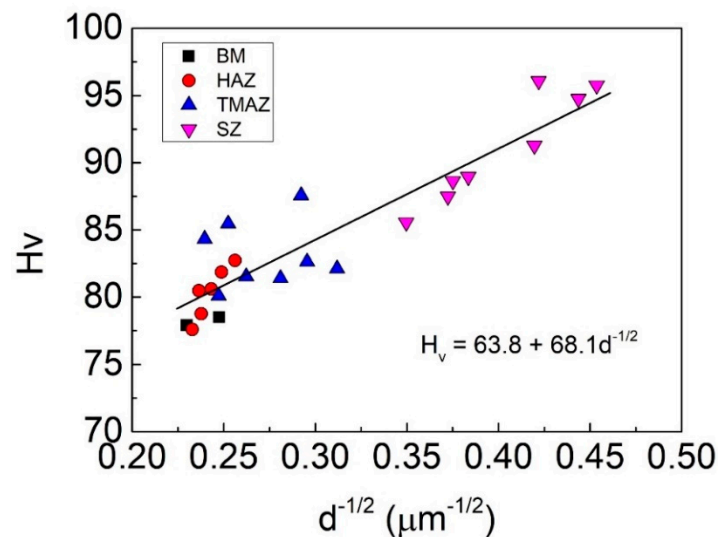

Figure 17. Evolution of microhardness for different joint regions (BM, HAZ, TMAZ and SZ) of the AA 5182 FSSW as a function of the inverse of the square root of the mean grain size representing the Hall–Petch relationship.

As can be noticed, Figure 17 demonstrates the validation of the Hall–Petch relationship. The extrapolated value for the friction hardness and slope of the Hall–Petch equation gives values of Hv_0 = 63.8 HV and k_H = 68.1 HV $\mu m^{1/2}$, respectively.

Indeed, the SZ is highly deformed but grain refinement occurs by DRX where the dislocations gradually transform into HAGB. The evolution of the microstructure of the HAZ and BM regions shows already weak dislocation density. Nevertheless, it seems that the values for the TMAZ slightly deviate compared to those for the HAZ and SZ due to the presence of deformation features as discussed in Section 4.1.2. In this zone, it can be assumed that grain size and dislocation density simultaneously participate in the hardening of the TMAZ region.

5. Conclusions

- Local microstructure and texture were evidenced in the upper and lower sheets through the shoulder dimension (10 mm) during the FSSW of the AA 5182 alloy.
- The upper sheet was mainly composed of the SZ and TMAZ due to the high deformation induced simultaneously by the tool rotation (shear deformation) and the shoulder download force (compression deformation), while the lower sheet was formed of the SZ, TMAZ, HAZ and BM due to the limited effect of the shoulder on the lower sheet.
- The change of the joint weld indicated that the right side undergoes more deformation than the left side.
- The formation of texture gradients is observed through the distance from the keyhole center, from shear-type texture at the SZ to plane strain compression deformation type texture at the TMAZ and then recrystallization texture at the HAZ and BM.
- The high temperature produced during FSSW seemed the origin of the development of recrystallization texture components such as Cube, Rotated-Cube, Goss and Rotated Goss in the SZ.
- Grain fragmentation and DDRX were evidenced in the TMAZ regions.
- The KAM approach demonstrated that the HAZ regions exhibit higher dislocation density than BM.
- The microhardness gradually decreases with increasing distance from the keyhole along the SZ, TMAZ and HAZ regions. However, the microhardness difference between the different zones is rather small, which may assure good deformation compatibility between the joint and the BM.
- The Hall–Petch constant was found valid through the weld zones with the fitting parameters $Hv_0 = 63.8$ HV and $k_H = 68.1$ HV $\mu m^{1/2}$.

Author Contributions: T.B.: conceptualization, methodology, validation, writing—original draft preparation, S.B.: conceptualization, investigation, F.B.: methodology, software, H.A.: conceptualization, validation, writing—original draft preparation writing—reviewing and editing. All authors have read and agreed to the published version of the manuscript.

Data Availability Statement: The data presented in this study are available on request from the corresponding author.

Conflicts of Interest: The authors declare no conflict of interest.

References

1. Zhang, W.; Xu, J. Advanced lightweight materials for Automobiles: A review. *Mater. Des.* **2022**, *221*, 110994. [CrossRef]
2. Toros, S.; Ozturk, F.; Kacar, I. Review of warm forming of aluminum–magnesium alloys. *J. Mater. Process. Technol.* **2008**, *207*, 1–12. [CrossRef]
3. Victor Christy, J.; Ismail Mourad, A.-H.; Sherif, M.M.; Shivamurthy, B. Review of recent trends in friction stir welding process of aluminum alloys and aluminum metal matrix composites. *Trans. Nonferrous Met. Soc. China* **2021**, *31*, 3281–3309. [CrossRef]
4. Thomas, W.M.; Johnson, K.I.; Wiesner, C.S. Friction Stir Welding—Recent Developments in Tool and Process Technologies. *Adv. Eng. Mater.* **2003**, *5*, 485–490. [CrossRef]
5. Besharati Givi, M.K.; Asadi, P. 1—General introduction. In *Advances in Friction-Stir Welding and Processing*; Givi, M.K.B., Asadi, P., Eds.; Woodhead Publishing: Sawston, UK, 2014; pp. 1–19.
6. Haghshenas, M.; Gerlich, A.P. Joining of automotive sheet materials by friction-based welding methods: A review. *Eng. Sci. Technol. Int. J.* **2018**, *21*, 130–148. [CrossRef]
7. El-Sayed, M.M.; Shash, A.Y.; Abd-Rabou, M.; ElSherbiny, M.G. Welding and processing of metallic materials by using friction stir technique: A review. *J. Adv. Join. Process.* **2021**, *3*, 100059. [CrossRef]
8. Prabhakar, D.A.P.; Shettigar, A.K.; Herbert, M.A.; Patel, G.C.M.; Pimenov, D.Y.; Giasin, K.; Prakash, C. A Comprehensive Review of Friction Stir Techniques in Structural Materials and Alloys: Challenges and Trends. *J. Mater. Res. Technol.* **2022**, *20*, 3025–3060. [CrossRef]
9. Baudin, T.; Brisset, F.; Zavdoveev, A.; Azzeddine, H. Microstructure and texture characterization in friction stir lap welded TIMETAL 21S. *Mater. Charact.* **2022**, *192*, 112216. [CrossRef]

10. Padhy, G.K.; Wu, C.S.; Gao, S. Friction stir based welding and processing technologies—Processes, parameters, microstructures and applications: A review. *J. Mater. Sci. Technol.* **2018**, *34*, 1–38. [CrossRef]
11. Liu, H.; Fujii, H. Microstructural and mechanical properties of a beta-type titanium alloy joint fabricated by friction stir welding. *Mater. Sci. Eng. A* **2018**, *711*, 140–148. [CrossRef]
12. Kumar, K.; Kailas, S.V. The role of friction stir welding tool on material flow and weld formation. *Mater. Sci. Eng. A* **2008**, *485*, 367–374. [CrossRef]
13. Bozzi, S.; Helbert-Etter, A.L.; Baudin, T.; Klosek, V.; Kerbiguet, J.G.; Criqui, B. Influence of FSSW parameters on fracture mechanisms of 5182 aluminium welds. *J. Mater. Process. Technol.* **2010**, *210*, 1429–1435. [CrossRef]
14. Yang, Q.; Mironov, S.; Sato, Y.S.; Okamoto, K. Material flow during friction stir spot welding. *Mater. Sci. Eng. A* **2010**, *527*, 4389–4398. [CrossRef]
15. Wang, D.A.; Lee, S.C. Microstructures and failure mechanisms of friction stir spot welds of aluminum 6061-T6 sheets. *J. Mater. Process. Technol.* **2007**, *186*, 291–297. [CrossRef]
16. Heidarzadeh, A.; Mironov, S.; Kaibyshev, R.; Çam, G.; Simar, A.; Gerlich, A.; Khodabakhshi, F.; Mostafaei, A.; Field, D.P.; Robson, J.D.; et al. Friction stir welding/processing of metals and alloys: A comprehensive review on microstructural evolution. *Prog. Mater. Sci.* **2021**, *117*, 100752. [CrossRef]
17. Ahmed, M.M.Z.; Wynne, B.P.; Rainforth, W.M.; Addison, A.; Martin, J.P.; Threadgill, P.L. Effect of Tool Geometry and Heat Input on the Hardness, Grain Structure, and Crystallographic Texture of Thick-Section Friction Stir-Welded Aluminium. *Metall. Mater. Trans. A* **2019**, *50*, 271–284. [CrossRef]
18. Fonda, R.W.; Bingert, J.F. Texture variations in an aluminum friction stir weld. *Scr. Mater.* **2007**, *57*, 1052–1055. [CrossRef]
19. Fonda, R.W.; Knipling, K.E. Texture development in friction stir welds. *Sci. Technol. Weld. Join.* **2011**, *16*, 288–294. [CrossRef]
20. Ahmed, M.M.Z.; Wynne, B.P.; Rainforth, W.M.; Threadgill, P.L. Through-thickness crystallographic texture of stationary shoulder friction stir welded aluminium. *Scr. Mater.* **2011**, *64*, 45–48. [CrossRef]
21. Shen, J.; Lage, S.B.M.; Suhuddin, U.F.H.; Bolfarini, C.; dos Santos, J.F. Texture Development and Material Flow Behavior During Refill Friction Stir Spot Welding of AlMgSc. *Metall. Mater. Trans. A* **2018**, *49*, 241–254. [CrossRef]
22. Liu, F.C.; Nelson, T.W. In-situ grain structure and texture evolution during friction stir welding of austenite stainless steel. *Mater. Des.* **2017**, *115*, 467–478. [CrossRef]
23. Liu, X.-c.; Zhen, Y.-q.; Sun, Y.-f.; Shen, Z.-k.; Chen, H.-y.; Guo, W.; Li, W.-y. Local inhomogeneity of mechanical properties in stir zone of friction stir welded AA1050 aluminum alloy. *Trans. Nonferrous Met. Soc. China* **2020**, *30*, 2369–2380. [CrossRef]
24. Moradi, M.M.; Jamshidi Aval, H.; Jamaati, R.; Amirkhanlou, S.; Ji, S. Microstructure and texture evolution of friction stir welded dissimilar aluminum alloys: AA2024 and AA6061. *J. Manuf. Process.* **2018**, *32*, 1–10. [CrossRef]
25. Sun, Y.; Fujii, H.; Takada, Y.; Tsuji, N.; Nakata, K.; Nogi, K. Effect of initial grain size on the joint properties of friction stir welded aluminum. *Mater. Sci. Eng. A* **2009**, *527*, 317–321. [CrossRef]
26. Xu, Y.; Ke, L.; Ouyang, S.; Mao, Y.; Niu, P. Precipitation behavior of intermetallic compounds and their effect on mechanical properties of thick plate friction stir welded Al/Mg joint. *J. Manuf. Process.* **2021**, *64*, 1059–1069. [CrossRef]
27. Morozova, I.; Królicka, A.; Obrosov, A.; Yang, Y.; Doynov, N.; Weiß, S.; Michailov, V. Precipitation phenomena in impulse friction stir welded 2024 aluminium alloy. *Mater. Sci. Eng. A* **2022**, *852*, 143617. [CrossRef]
28. Suhuddin, U.F.H.R.; Mironov, S.; Sato, Y.S.; Kokawa, H. Grain structure and texture evolution during friction stir welding of thin 6016 aluminum alloy sheets. *Mater. Sci. Eng. A* **2010**, *527*, 1962–1969. [CrossRef]
29. Bozzi, S.; Helbert-Etter, A.L.; Baudin, T.; Criqui, B.; Kerbiguet, J.G. Intermetallic compounds in Al 6016/IF-steel friction stir spot welds. *Mater. Sci. Eng. A* **2010**, *527*, 4505–4509. [CrossRef]
30. Etter, A.L.; Bozzi, S.; Baudin, T. Dynamic Recrystallization in Similar 5182 Al/Al and Dissimilar Al/Fe Friction Stir Spot Welds. *Mater. Sci. Forum* **2012**, *715–716*, 152–157. [CrossRef]
31. Patterson, E.E.; Hovanski, Y.; Field, D.P. Microstructural Characterization of Friction Stir Welded Aluminum-Steel Joints. *Metall. Mater. Trans. A* **2016**, *47*, 2815–2829. [CrossRef]
32. Imam, M.; Racherla, V.; Biswas, K.; Fujii, H.; Chintapenta, V.; Sun, Y.; Morisada, Y. Microstructure-property relation and evolution in friction stir welding of naturally aged 6063 aluminium alloy. *Int. J. Adv. Manuf. Technol.* **2017**, *91*, 1753–1769. [CrossRef]
33. Basak, S.; Mondal, M.; Gao, K.; Hong, S.-T.; Anaman, S.Y.; Cho, H.-H. Friction stir butt-welding of roll cladded aluminum thin sheets: Effect of microstructural and texture changes on mechanical properties. *Mater. Sci. Eng. A* **2022**, *832*, 142490. [CrossRef]
34. Zhou, C.; Yang, X.; Luan, G. Fatigue properties of friction stir welds in Al 5083 alloy. *Scr. Mater.* **2005**, *53*, 1187–1191. [CrossRef]
35. Su, P.; Gerlich, A.; North, T.H.; Bendzsak, G.J. Material flow during friction stir spot welding. *Sci. Technol. Weld. Join.* **2006**, *11*, 61–71. [CrossRef]
36. Hirata, T.; Oguri, T.; Hagino, H.; Tanaka, T.; Chung, S.W.; Takigawa, Y.; Higashi, K. Influence of friction stir welding parameters on grain size and formability in 5083 aluminum alloy. *Mater. Sci. Eng. A* **2007**, *456*, 344–349. [CrossRef]
37. Bozzi, S.; Etter, A.L.; Baudin, T.; Robineau, A.; Goussain, J.C. Dynamic Recrystallization Mechanisms on Spot Welding of 6008 Aluminium Alloy to Steel by Friction Stir Welding. *Mater. Sci. Forum* **2007**, *558–559*, 477–483. [CrossRef]
38. Bozzi, S. Optimisation du Procédé FSSW (Friction Stir Spot Welding) Pour des Assemblages Homogènes Al/Al et Hétérogènes Al/Acier. Ph.D. Thesis, Université Paris-Sud, Orsay, France, 2009.
39. Zhang, Z.; Yang, X.; Zhang, J.; Zhou, G.; Xu, X.; Zou, B. Effect of welding parameters on microstructure and mechanical properties of friction stir spot welded 5052 aluminum alloy. *Mater. Des.* **2011**, *32*, 4461–4470. [CrossRef]

40. Gratecap, F.; Girard, M.; Marya, S.; Racineux, G. Exploring material flow in friction stir welding: Tool eccentricity and formation of banded structures. *Int. J. Mater. Form.* **2012**, *5*, 99–107. [CrossRef]

41. Oladimeji, O.O.; Taban, E.; Kaluc, E. Understanding the role of welding parameters and tool profile on the morphology and properties of expelled flash of spot welds. *Mater. Des.* **2016**, *108*, 518–528. [CrossRef]

42. Li, Z.; Yue, Y.; Ji, S.; Peng, C.; Wang, L. Optimal design of thread geometry and its performance in friction stir spot welding. *Mater. Des.* **2016**, *94*, 368–376. [CrossRef]

43. Chu, Q.; Hao, S.J.; Li, W.Y.; Yang, X.W.; Zou, Y.F.; Wu, D. Impact of shoulder morphology on macrostructural forming and the texture development during probeless friction stir spot welding. *J. Mater. Res. Technol.* **2021**, *12*, 2042–2054. [CrossRef]

44. Tiwan; Ilman, M.N.; Kusmono; Sehono. Microstructure and mechanical performance of dissimilar friction stir spot welded AA2024-O/AA6061-T6 sheets: Effects tool rotation speed and pin geometry. *Int. J. Lightweight Mater. Manuf.* **2022**, *6*, 1–14. [CrossRef]

45. Furukawa, M.; Horita, Z.; Nemoto, M.; Valiev, R.Z.; Langdon, T.G. Factors influencing the flow and hardness of materials with ultrafine grain sizes. *Philos. Mag. A* **1998**, *78*, 203–216. [CrossRef]

46. Armstrong, R.W. Engineering science aspects of the Hall–Petch relation. *Acta Mech.* **2014**, *225*, 1013–1028. [CrossRef]

47. Mikami, Y.; Oda, K.; Kamaya, M.; Mochizuki, M. Effect of reference point selection on microscopic stress measurement using EBSD. *Mater. Sci. Eng. A* **2015**, *647*, 256–264. [CrossRef]

48. Liu, H.; Ushioda, K.; Fujii, H. Elucidation of microstructural evolution of beta-type titanium alloy joint during friction stir welding using liquid CO_2 cooling. *Mater. Charact.* **2018**, *145*, 490–500. [CrossRef]

49. Cho, J.-H.; Rollett, A.D.; Oh, K.H. Determination of a mean orientation in electron backscatter diffraction measurements. *Metall. Mater. Trans. A* **2005**, *36*, 3427–3438. [CrossRef]

50. Azzeddine, H.; Bourezg, Y.I.; Khereddine, A.Y.; Baudin, T.; Helbert, A.-L.; Brisset, F.; Kawasaki, M.; Bradai, D.; Langdon, T.G. An investigation of the stored energy and thermal stability in a Cu–Ni–Si alloy processed by high-pressure torsion. *Philos. Mag.* **2020**, *100*, 688–712. [CrossRef]

51. Bachmann, F.; Hielscher, R.; Schaeben, H. Texture Analysis with MTEX—Free and Open Source Software Toolbox. *Solid State Phenom.* **2010**, *160*, 63–68. [CrossRef]

52. Azzeddine, H.; Bradai, D.; Baudin, T.; Langdon, T.G. Texture evolution in high-pressure torsion processing. *Prog. Mater. Sci.* **2022**, *125*, 100886. [CrossRef]

53. Engler, O.; Hirsch, J. Texture control by thermomechanical processing of AA6xxx Al–Mg–Si sheet alloys for automotive applications—A review. *Mater. Sci. Eng. A* **2002**, *336*, 249–262. [CrossRef]

54. Hamad, K.; Yang, H.W.; Ko, Y.G. Interpretation of annealing texture changes of severely deformed Al-Mg-Si alloy. *J. Alloys Compd.* **2016**, *687*, 300–305. [CrossRef]

55. Zhang, K.; He, Q.; Rao, J.H.; Wang, Y.; Zhang, R.; Yuan, X.; Feng, W.; Huang, A. Correlation of textures and hemming performance of an AA6XXX aluminium alloy. *J. Alloys Compd.* **2021**, *853*, 157081. [CrossRef]

56. Li, S.; Sun, F.; Li, H. Observation and modeling of the through-thickness texture gradient in commercial-purity aluminum sheets processed by accumulative roll-bonding. *Acta Mater.* **2010**, *58*, 1317–1331. [CrossRef]

57. Nandan, R.; DebRoy, T.; Bhadeshia, H.K.D.H. Recent advances in friction-stir welding—Process, weldment structure and properties. *Prog. Mater. Sci.* **2008**, *53*, 980–1023. [CrossRef]

58. Piccini, J.M.; Svoboda, H.G. Effect of pin length on Friction Stir Spot Welding (FSSW) of dissimilar Aluminum-steel joints. *Procedia Mater. Sci.* **2015**, *9*, 504–513. [CrossRef]

59. Shekhawat, R.S.; Nadakuduru, V.N. Impact of post weld heat treatment on mechanical and microstructural properties of underwater friction stir spot welded 6061 aluminium alloy. *Mater. Today: Proc.* **2022**, *56*, 2647–2652. [CrossRef]

60. Ahmed, M.M.Z.; El-Sayed Seleman, M.M.; Ahmed, E.; Reyad, H.A.; Touileb, K.; Albaijan, I. Friction Stir Spot Welding of Different Thickness Sheets of Aluminum Alloy AA6082-T6. *Materials* **2022**, *15*, 2971. [CrossRef] [PubMed]

61. Akinlabi, E.T.; Ikumapayi, O.M.; Osinubi, A.S.; Madushele, N.; Abegunde, O.O.; Fatoba, S.O.; Akinlabi, S.A. Characterizations of AA5083-H116 produced by friction stir spot welding technique. *Adv. Mater. Process. Technol.* **2022**, *8*, 2299–2313. [CrossRef]

62. Donatus, U.; Thompson, G.E.; Zhou, X.; Wang, J.; Beamish, K. Flow patterns in friction stir welds of AA5083 and AA6082 alloys. *Mater. Des.* **2015**, *83*, 203–213. [CrossRef]

63. Tongne, A.; Jahazi, M.; Feulvarch, E.; Desrayaud, C. Banded structures in friction stir welded Al alloys. *J. Mater. Process. Technol.* **2015**, *221*, 269–278. [CrossRef]

64. Chen, Z.W.; Cui, S. On the forming mechanism of banded structures in aluminium alloy friction stir welds. *Scr. Mater.* **2008**, *58*, 417–420. [CrossRef]

65. Xu, S.; Deng, X. A study of texture patterns in friction stir welds. *Acta Mater.* **2008**, *56*, 1326–1341. [CrossRef]

66. Yoon, T.-J.; Yun, J.-G.; Kang, C.-Y. Formation mechanism of typical onion ring structures and void defects in friction stir lap welded dissimilar aluminum alloys. *Mater. Des.* **2016**, *90*, 568–578. [CrossRef]

67. Yashin, V.; Aryshenskii, E.; Hirsch, J.; Konovalov, S.; Latushkin, I. Study of recrystallization kinetics in AA5182 aluminium alloy after deformation of the as-cast structure. *Mater. Res. Express* **2019**, *6*, 066552. [CrossRef]

68. Liu, W.C.; Zhai, T.; Morris, J.G. Comparison of recrystallization and recrystallization textures in cold-rolled DC and CC AA 5182 aluminum alloys. *Mater. Sci. Eng. A* **2003**, *358*, 84–93. [CrossRef]

69. Zhang, J.X.; Ma, M.; Liu, W.C. Effect of initial grain size on the recrystallization and recrystallization texture of cold-rolled AA 5182 aluminum alloy. *Mater. Sci. Eng. A* **2017**, *690*, 233–243. [CrossRef]
70. Sakai, T.; Belyakov, A.; Kaibyshev, R.; Miura, H.; Jonas, J.J. Dynamic and post-dynamic recrystallization under hot, cold and severe plastic deformation conditions. *Prog. Mater. Sci.* **2014**, *60*, 130–207. [CrossRef]
71. Branger, V.; Mathon, M.H.; Baudin, T.; Penelle, R. "In-situ" neutron diffraction study of the cube crystallographic texture development in Fe53%-Ni alloy during recrystallization. *Scr. Mater.* **2000**, *43*, 325–330. [CrossRef]
72. Etter, A.L.; Mathon, M.H.; Baudin, T.; Branger, V.; Penelle, R. Influence of the cold rolled reduction on the stored energy and the recrystallization texture in a Fe–53%Ni alloy. *Scr. Mater.* **2002**, *46*, 311–317. [CrossRef]
73. Ateba Betanda, Y.; Helbert, A.-L.; Brisset, F.; Mathon, M.-H.; Waeckerlé, T.; Baudin, T. Measurement of stored energy in Fe–48%Ni alloys strongly cold-rolled using three approaches: Neutron diffraction, Dillamore and KAM approaches. *Mater. Sci. Eng. A* **2014**, *614*, 193–198. [CrossRef]
74. Azzeddine, H.; Tirsatine, K.; Baudin, T.; Mathon, M.-H.; Helbert, A.-L.; Brisset, F.; Bradai, D. On the stored energy evolution after accumulative roll-bonding of invar alloy. *Mater. Chem. Phys.* **2017**, *201*, 408–415. [CrossRef]
75. Kestens, L.A.I.; Pirgazi, H. Texture formation in metal alloys with cubic crystal structures. *Mater. Sci. Technol.* **2016**, *32*, 1303–1315. [CrossRef]
76. Starink, M.J.; Cheng, X.; Yang, S. Hardening of pure metals by high-pressure torsion: A physically based model employing volume-averaged defect evolutions. *Acta Mater.* **2013**, *61*, 183–192. [CrossRef]